J. Fluid Mech. (2014), *vol.* 745, *pp.* 682–715.
doi:10.1017/jfm.2014.90

Viscous film flow coating the interior of a vertical tube. Part 1. Gravity-driven flow

Roberto Camassa[1], **H. Reed Ogrosky**[2,†] **and Jeffrey Olander**[3]

[1]Carolina Center for Interdisciplinary Applied Mathematics, Department of Mathematics, University of North Carolina, Chapel Hill, NC 27599-3250, USA

[2]Department of Mathematics, University of Wisconsin-Madison, Madison, WI 53706-1325, USA

[3]Department of Physics, University of North Carolina, Chapel Hill, NC 27599-3255, USA

(Received 18 July 2013; revised 22 November 2013; accepted 11 February 2014; first published online 25 March 2014)

The gravity-driven flow of a viscous liquid film coating the inside of a tube is studied both theoretically and experimentally. As the film moves downward, small perturbations to the free surface grow due to surface tension effects and can form liquid plugs. A first-principles strongly nonlinear model based on long-wave asymptotics is developed to provide simplified governing equations for the motion of the film flow. Linear stability analysis on the basic solution of the model predicts the speed and wavelength of the most unstable mode, and whether the film is convectively or absolutely unstable. These results are found to be in remarkable agreement with the experiments. The model is also solved numerically to follow the time evolution of instabilities. For relatively thin films, these instabilities saturate as a series of small-amplitude travelling waves, while thicker films lead to solutions whose amplitude becomes large enough for the liquid surface to approach the centre of the tube in finite time, suggesting liquid plug formation. Next, the model's periodic travelling wave solutions are determined by a continuation algorithm using the results from the time evolution code as initial seed. It is found that bifurcation branches for these solutions exist, and the critical turning points where branches merge determine film mean thicknesses beyond which no travelling wave solutions exist. These critical thickness values are in good agreement with those for liquid plug formations determined experimentally and numerically by the time-evolution code.

Key words: instability, interfacial flows (free surface), thin films

1. Introduction

The flow of a viscous fluid film coating the inner or outer wall of a vertical cylinder has received much attention over the last two decades, motivated by various engineering and biological applications. For instance, some of the studies of the exterior case originated from the need to understand the nature of instability growth during the process of coating fibres (and we will henceforth refer to this as the exterior or 'fibre' case), while the interior case is of interest to the understanding of mucus dynamics in human airways.

† Email address for correspondence: ogrosky@math.wisc.edu

When the liquid film is a Newtonian fluid, the typical mathematical set-up is that of an initial-boundary-value problem for the Navier–Stokes equations. The general presence of a free surface where the fluid is in contact with ambient air makes even the simplest case fairly challenging from a mathematical perspective, and to make progress it is often useful to consider models that incorporate a class of simplifying assumptions. In fact, even when exact solutions to the Navier–Stokes equations for such flows can be found, basically exploiting the linearization of these equations for parallel flows, it is often the case that these solutions are unstable to small perturbations and hence of potentially limited practical interest (see e.g. Goren 1962 and Yih 1967 for an analysis of instability to long-wave perturbations). Physically, the instability growth originates from the interplay of flow characteristics, liquid surface tension and curvature of the free surface, and is akin to instability growth in liquid jets where the free surface pinches off to form droplets. Several modelling approaches have been developed to explore the behaviour of fluid film flows. Fully nonlinear models of such flows, where no assumption is made on the magnitude of the free-surface displacement from a reference configuration, can be loosely categorized into three groups: (i) thin-film asymptotic models, (ii) long-wave asymptotic models, and (iii) integral models. This last category has been developed to examine flows with moderate Reynolds number by departing from the traditional long-wave expansion when calculating the first- and second-order corrections; see e.g. Craster & Matar (2009) for a review of these modelling developments. As we are primarily interested here in low-Reynolds-number flows, we focus instead on developments in the first two categories.

Thin-film asymptotic models are derived by exploiting the ratio of film thickness to cylinder thickness, and a single evolution equation can be found for the location of the fluid–air interface. An extensive literature exists on this approach. For instance, Hammond (1983) considered the growth of instabilities driven by capillary forces in a thin film with cylindrical geometry and studied the formation of collars and lobes. Frenkel (1992) derived an evolution equation that included the effects of gravity, and his model is valid for both interior and exterior coatings. This model was studied by Kerchman & Frenkel (1994) and Kalliadasis & Chang (1994), who noted the possibility of finite-time blow-up of its solutions, and studied its behaviour near blow-up under a self-similarity assumption.

Long-wave models, which exploit the ratio of film thickness to wavelength, have also been studied for quite some time, see e.g. Lin & Liu (1975) for both the interior and exterior coating set-up. This approach has been used to derive a long-wave model for the related problem of air-driven interior film flow by Camassa & Lee (2006), and a similar procedure will be studied here.

Exterior coating flows have enjoyed most of the attention in recent years due to their numerous industrial applications. From a mathematical modelling perspective these flows are closely related, albeit with important differences, to interior coatings, so we first briefly review models designed solely for exterior films. Roy, Roberts & Simpson (2002) developed a thin-film model which conserves mass, unlike Frenkel (1992). Kliakhandler, Davis & Bankoff (2001) and Craster & Matar (2006) both developed long-wave models for the exterior coating case. The derivation of the model in Kliakhandler *et al.* (2001) is tailored around a few simplifying assumptions without resorting to a systematic asymptotic expansion, and the resulting single evolution equation is virtually identical to the model asymptotically derived by Craster & Matar (2006). The derivation of this latter model is based not only on long-wave asymptotics but also on small Bond numbers, whereby the Bond number

is tied to the long-wave small parameter. Experiments performed by Smolka, North & Guerra (2008) have shown that this model is effective in describing the linear stability of an exterior film flow with low to moderate Reynolds number.

Perhaps the most critical difference between film behaviour in the exterior and interior cases is that with interior coatings, if the film is thick enough, instabilities can grow unchecked until they pinch off and form a liquid plug or bridge. Lister *et al.* (2006) used the Hammond equation to study the behaviour of liquid collars and lobes without the effects of gravity. Jensen (2000) studied the tendency of draining liquid collars to form plugs using the model by Frenkel (1992), and found a critical modified Bond number below which plugs form. Once a plug has formed, its movement driven with either prescribed constant velocity or by a constant pressure gradient has been studied numerically by Campana *et al.* (2007) and Ubal *et al.* (2008), respectively. The tendency of a plug to thin or thicken in these cases is studied along with the quasi-steady streamlines pattern within the fluid. Other theoretical studies have focused on plug behaviour in other geometries, including a channel (Suresh & Grotberg 2005) and flexible tube (Halpern & Grotberg 1992).

In this work we develop and use long-wave asymptotic models to study the gravity-driven flow of a viscous film down the interior wall of a vertical cylinder. We limit ourselves to low-Reynolds-number regimes, but do not restrict the thickness of the film or the values of the Bond number, and compare with the corresponding exact results from the appropriate Stokes (viscous-dominated) governing equations whenever these can be obtained. Further, we present the data collected from our experimental investigation, and compare them with the results of linear analysis and numerical solutions to the low-Reynolds-number model we derive. The model is shown to perform effectively in predicting important features of the flow, such as liquid plug formation and whether free-surface instabilities are absolute or convective. We also refer back to the better known case of an exterior film when appropriate. Specifically, the paper is organized as follows. In § 2 we derive three models according to their asymptotic ordering, with or without first-order inertial effects. These models are compared with known ones from the literature, as well as shown to reduce to these in the appropriate limits. Next, a series of experiments are performed and presented in § 3. We perform a linear stability analysis from both a temporal and spatial viewpoint in § 4, and verify its predictions against the experimental data. In § 5 we discuss numerical solutions to the first-order long-wave model, and develop algorithms to find travelling wave solutions and discuss their properties. Further comparisons to experimental observations are made with the time-dependent evolution of numerical solutions. A discussion of the results is contained in § 6, as is a brief discussion of the case where the air in the core region of the tube is forced to flow by a pressure gradient, which is the subject of Part 2 of this work. Some details of the model derivation are given in the appendix.

2. Long-wave asymptotic models

We consider a liquid film flow governed by the incompressible axisymmetric Navier–Stokes equations in cylindrical coordinates,

$$\left.\begin{aligned} \rho(\bar{u}_{\bar{t}} + \bar{u}\bar{u}_{\bar{r}} + \bar{w}\bar{u}_{\bar{z}}) &= -\bar{p}_{\bar{r}} + \mu\left(\frac{1}{\bar{r}}\partial_{\bar{r}}(\bar{r}\bar{u}_{\bar{r}}) + \bar{u}_{\bar{z}\bar{z}} - \frac{\bar{u}}{\bar{r}^2}\right), \\ \rho(\bar{w}_{\bar{t}} + \bar{u}\bar{w}_{\bar{r}} + \bar{w}\bar{w}_{\bar{z}}) &= -\bar{p}_{\bar{z}} + \mu\left(\frac{1}{\bar{r}}\partial_{\bar{r}}(\bar{r}\bar{w}_{\bar{r}}) + \bar{w}_{\bar{z}\bar{z}}\right) + \rho g, \\ \frac{1}{\bar{r}}\partial_{\bar{r}}(\bar{r}\bar{u}) + \bar{w}_{\bar{z}} &= 0, \end{aligned}\right\} \tag{2.1}$$

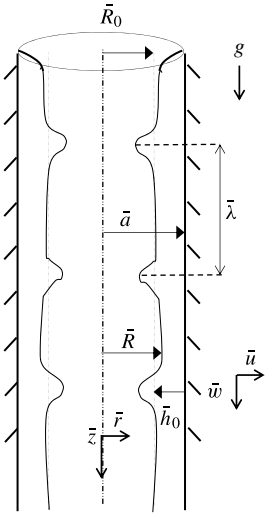

FIGURE 1. Sketch of the flow configuration and variable definitions.

where the velocity components $(\bar{u}, \bar{v}, \bar{w})$ correspond to the coordinates $(\bar{r}, \bar{\theta}, \bar{z})$. Here the axial coordinate $\bar{z}$ increases in the downward direction along the tube. Other notation is pressure $\bar{p}$, density ρ, molecular viscosity μ, and gravity acceleration g; see figure 1 for a sketch of the set-up. Overbars denote dimensional quantities and subscripts denote partial derivatives. Boundary conditions at the wall $\bar{r} = \bar{a}$ are no-slip

$$\bar{u} = \bar{w} = 0, \tag{2.2}$$

while at the free surface $\bar{r} = \bar{R}(\bar{z}, \bar{t})$ continuity of tangential stress

$$(\bar{w}_{\bar{r}} + \bar{u}_{\bar{z}})(1 - \bar{R}_{\bar{z}}^2) + 2(\bar{u}_{\bar{r}} - \bar{w}_{\bar{z}})\bar{R}_{\bar{z}} = 0, \tag{2.3}$$

and jump in normal stress according to the Young–Laplace equation,

$$\begin{aligned}(-\bar{p} + \bar{p}^{(g)})(1 + \bar{R}_{\bar{z}}^2) + 2\mu(\bar{u}_{\bar{r}} + \bar{w}_{\bar{z}}\bar{R}_{\bar{z}}^2) + \mu\bar{R}_{\bar{z}}(\bar{w}_{\bar{r}} + \bar{u}_{\bar{z}}) \\ = \gamma(1 + \bar{R}_{\bar{z}}^2)\left(\frac{1}{\bar{R}(1 + \bar{R}_{\bar{z}}^2)^{1/2}} - \frac{\bar{R}_{\bar{z}\bar{z}}}{(1 + \bar{R}_{\bar{z}}^2)^{3/2}}\right),\end{aligned} \tag{2.4}$$

are required. Here $\bar{p}^{(g)}$ is the background pressure, γ is surface tension and the sign of the left-hand side of (2.4) is opposite that of the exterior case. To these dynamical conditions, a kinematic boundary equation needs to be added at $\bar{r} = \bar{R}$,

$$\bar{u} = \bar{R}_{\bar{t}} + \bar{w}\bar{R}_{\bar{z}}. \tag{2.5}$$

Denoting the length of a typical disturbance to the free surface by $\bar{\lambda}$, the dynamics is selected by the experimental parameters $\rho, g, \mu, \gamma, \bar{a}, \bar{\lambda}$ and the mean thickness of the film $\bar{h}_0 = \bar{a} - \bar{R}_0$. These can be combined into four dimensionless parameters: (1) the Reynolds number, $Re = \rho^2 g \bar{h}_0^3/\mu^2$, (2) the Bond number $Bo = \rho g \bar{h}_0^2/\gamma$, (3) a film thickness parameter $a = \bar{a}/\bar{h}_0$ and (4) an aspect ratio $\epsilon = \bar{h}_0/\bar{\lambda}$. Flows with matching parameters can be expected to be dynamically similar. Other dimensionless parameters

appearing in studies of gravity-driven film flows in lieu of the Bond number are the Weber number, $We = Bo \times Re$, and the Kapitza number, $Ka = \gamma\rho^{1/3}/\mu^{4/3}g^{1/3}$. The Kapitza number offers the advantage that it is determined only by the properties of the fluid and does not depend on the flow rate or film thickness; however, as all of the models in the literature which are discussed here were derived with reference to the Bond (or Weber) number, we adopt this convention as well for ease of comparison. The value of Ka for the fluid used in the experiments reported here will be discussed in § 3.

2.1. *Leading-order flow*

There is an exact 'parallel flow' solution to (2.1)–(2.5) which is a balance of viscous forces and gravity with a free surface given by $\bar{R}(\bar{z}, \bar{t}) = \bar{R}_0$, where the only non-zero velocity component is the axial component ($\bar{w}$), and the only non-zero gradient component is the radial one ($\partial_{\bar{r}}$),

$$\bar{w} = \frac{\rho g}{4\mu}\left(\bar{a}^2 - \bar{r}^2 + 2\bar{R}_0^2 \log\frac{\bar{r}}{\bar{a}}\right). \tag{2.6}$$

(When $\bar{R}_0 = 0$, i.e. for a tube entirely filled with liquid, the velocity profile reduces to that of Poiseuille pipe flow.) Goren (1962) studied the stability of such flows; for fluids with high viscosity like those considered here, the free surface is unstable to a range of small wavenumbers. Motivated by these long-wave instabilities, we seek to model the flow using long-wave asymptotics.

Proceeding with the traditional long-wave asymptotic approach, we take $\epsilon \ll 1$. We then non-dimensionalize (2.1) with

$$\left.\begin{aligned} r = \bar{r}/\bar{h}_0, \quad z = \bar{z}/\bar{\lambda}, \quad u = \bar{u}/\overline{U}_0, \\ w = \bar{w}/\overline{W}_0, \quad t = \bar{t}\overline{W}_0/\bar{\lambda}, \quad p = \bar{p}\bar{h}_0/(\mu\overline{W}_0), \end{aligned}\right\} \tag{2.7}$$

where $\overline{W}_0 = \rho g\bar{h}_0^2/\mu$ is the axial velocity scale and $\overline{U}_0 = \epsilon\overline{W}_0$, giving

$$\epsilon^2 Re(u_t + uu_r + wu_z) = -p_r + \epsilon\left(\frac{1}{r}\partial_r(ru_r) + \epsilon^2 u_{zz} - \frac{u}{r^2}\right), \tag{2.8}$$

$$\epsilon Re(w_t + uw_r + ww_z) = -\epsilon p_z + \frac{1}{r}\partial_r(rw_r) + \epsilon^2 w_{zz} + 1, \tag{2.9}$$

$$\frac{1}{r}\partial_r(ru) + w_z = 0. \tag{2.10}$$

The boundary condition (2.2) at the wall is

$$w = 0, \quad u = 0, \tag{2.11}$$

while at the interface $r = R(z, t)$ the boundary conditions (2.3)–(2.5) become

$$(w_r + \epsilon^2 u_z)(1 - (\epsilon R_z)^2) + 2\epsilon^2(u_r - w_z)R_z = 0, \tag{2.12}$$

$$\begin{aligned}(-p + p^{(g)})(1 + (\epsilon R_z)^2) + 2\epsilon(u_r + w_z(\epsilon R_z)^2) + \epsilon R_z(w_r + \epsilon^2 u_z) \\ = \frac{1 + (\epsilon R_z)^2}{Bo}\left(\frac{1}{R(1 + (\epsilon R_z)^2)^{1/2}} - \frac{\epsilon^2 R_{zz}}{(1 + (\epsilon R_z)^2)^{3/2}}\right),\end{aligned} \tag{2.13}$$

$$u = R_t + wR_z, \tag{2.14}$$

respectively. Integrating the continuity equation (2.10) across the fluid layer and then substituting the kinematic boundary condition (2.14) yields a layer-averaged mass conservation equation,

$$R_t = \frac{1}{R}\frac{\partial}{\partial z}\int_R^a w\, r\, \mathrm{d}r. \tag{2.15}$$

With an approximate expression for w, this constitutes a single decoupled equation describing the interfacial evolution. Note that after multiplying by R, mass conservation is seen mathematically by (2.15) as a conservation law for the quantity R^2. Thus the models we derive below conserve equivalently mass or volume, since the liquid is assumed incompressible.

As with the full governing equations, the four dimensionless parameters Re, Bo, a and ϵ appear in (2.8)–(2.15). We pause to consider the relative sizes of the parameters for the experiments conducted here. Due to the high viscosity of the oil employed in all our experiments, the Reynolds number of the flows studied here is $Re = O(10^{-2})$ or lower. Thus in the asymptotic limit $\epsilon \to 0$ we will also take $\epsilon Re \to 0$. The Bond number, however, is as large as $Bo = O(1)$ in our experiments and no restrictions will be made on its size in the model equations. We shall not restrict the size of the parameter a, in contrast to the thin-film models (which we will discuss in § 2.4). For most of the experiments considered here, the aspect ratio ϵ is less than 0.2, though for the thickest films examined ϵ takes values as high as 0.5.

We now seek solutions as regular perturbation expansions in ϵ for the velocities and pressure, i.e.

$$\left.\begin{aligned} u &= u_0 + \epsilon u_1 + \cdots, \\ w &= w_0 + \epsilon w_1 + \cdots, \\ p &= p_0 + \epsilon p_1 + \cdots, \end{aligned}\right\} \tag{2.16}$$

and substitute these expansions into the motion (2.8)–(2.13). Taking the limit $\epsilon \to 0$ yields at leading order

$$0 = p_{0r}, \quad \frac{1}{r}\partial_r(rw_{0r}) = -1, \quad \frac{1}{r}\partial_r(ru_0) + w_{0z} = 0, \tag{2.17}$$

with boundary conditions at the wall

$$u_0 = w_0 = 0, \tag{2.18}$$

and at the interface

$$w_{0r} = 0, \quad p_0 = -\frac{1}{Bo}\left(\frac{1}{R} - \epsilon^2 R_{zz}\right), \tag{2.19}$$

where we have set the overall constant background pressure to zero without loss of generality. The terms in parentheses in (2.19) model the role that surface tension plays through the two types of curvature in an axisymmetric film, namely the azimuthal and axial curvature. Note that the axial curvature has been retained despite being $O(\epsilon^2)$. This term is traditionally kept in modelling of liquid films (see e.g. Oron, Davis & Bankoff 1997 and Craster & Matar 2009 for a discussion of this term's role). We note that solutions to the leading-order model derived below will in general tend to

form shocks, so that higher-order derivatives must eventually play a prominent role in the film's evolution, no matter how smooth the initial conditions. This capillary term appears to be the lowest-order one in the long-wave asymptotics with the ability to prevent shock formation; it can thus be expected to play a dominant role with respect to its counterparts of similar or lower order. The higher-order terms in the asymptotic expansion computed below further corroborate this interpretation of the capillary contribution to the asymptotic model.

The solution to (2.17)–(2.19) is given by

$$u_0 = -RR_z\left(\frac{r}{2}\log\frac{r}{a} - \frac{r}{4} + \frac{a^2}{4r}\right), \tag{2.20}$$

$$w_0 = \frac{1}{4}(a^2 - r^2) + \frac{R^2}{2}\log\frac{r}{a}, \tag{2.21}$$

$$p_0 = -\frac{1}{Bo}\left(\frac{1}{R} - \epsilon^2 R_{zz}\right), \tag{2.22}$$

where (2.21) is the non-dimensional form of the exact solution (2.6) in the case of a flat free surface. Substituting (2.21) into (2.15) yields a leading-order model representing the base flow given by

$$R_t = \frac{1}{2}\left(R^2 - a^2 - 2R^2\log\frac{R}{a}\right)R_z. \tag{2.23}$$

It is readily seen that the flat solution $R = R_0$ (with velocity profile given by (2.21)) simultaneously solves the governing equations (2.8)–(2.14) and the model equation (2.23).

2.2. *First-order corrections*

At $O(\epsilon)$, the momentum equations are

$$p_{1r} = \frac{1}{r}\partial_r(ru_{0r}) - u_0/r^2, \tag{2.24}$$

$$\frac{1}{r}\partial_r(rw_{1r}) = Re(w_{0t} + u_0 w_{0r} + w_0 w_{0z}) + p_{0z}, \tag{2.25}$$

$$\frac{1}{r}\partial_r(ru_1) + w_{1z} = 0. \tag{2.26}$$

Boundary conditions at the wall are

$$u_1 = w_1 = 0, \tag{2.27}$$

and at the interface

$$w_{1r} = 0, \quad p_1 = 2u_{0r}. \tag{2.28}$$

In order to solve (2.25) we use (2.23) to approximate w_{0t}; the solution to (2.24)–(2.28) is given in the appendix. The interfacial evolution equation with first-order corrections is then

$$R_t = \frac{1}{R}\frac{\partial}{\partial z}\int_R^a (w_0 + \epsilon w_1) r\,\mathrm{d}r, \tag{2.29}$$

which can be written as

$$R_t = f_1(R;a)R_z + \frac{\epsilon}{R}\left[Sf_2(R;a)(R_z + \epsilon^2 R^2 R_{zzz}) + Ref_3(R;a)R_z\right]_z, \tag{2.30}$$

where

$$\left.\begin{aligned} f_1(R;a) &= \frac{1}{2}[R^2 - a^2 - 2R^2\log(R/a)], \\ f_2(R;a) &= -\frac{a^4}{R^2} + 4a^2 - 3R^2 + 4R^2\log\frac{R}{a}, \\ f_3(R;a) &= \left[-\frac{59}{48}R^7 + \frac{15}{16}a^2R^5 + \frac{9}{16}a^4R^3 - \frac{13}{48}a^6R + \frac{17}{4}a^2R^5\log(R/a)\right. \\ &\quad -\frac{7}{4}a^4R^3\log(R/a) + \frac{5}{2}R^7(\log(R/a))^2 - \frac{5}{2}a^2R^5(\log(R/a))^2 \\ &\quad \left. -2R^7(\log(R/a))^3\right], \end{aligned}\right\} \tag{2.31}$$

and $S = 1/16Bo$.

The model (2.30) is nearly identical to that derived by Lin & Liu (1975), as well as that derived by Camassa & Lee (2006) for the liquid phase. Lin & Liu (1975) performed linear stability analysis of their long-wave model and did not retain the full form of the curvature terms; also our $f_3(R;a)$ differs from theirs in one coefficient, an apparent typo.

Since the Reynolds number of the flows studied here is $Re = O(10^{-2})$ or lower, we choose to neglect the inertial terms, in which case the first-order model reduces to

$$R_t = f_1(R;a)R_z + \frac{\epsilon S}{R}\left[f_2(R;a)(R_z + \epsilon^2 R^2 R_{zzz})\right]_z. \tag{2.32}$$

As noted earlier, both models (2.30) and (2.32) are essentially statements of mass conservation, as (2.32) can be equivalently rewritten as

$$8(R^2)_t = \{f_2(R;a)[-R^2 + 16\epsilon S(R_z + \epsilon^2 R^2 R_{zzz})]\}_z. \tag{2.33}$$

The flat solution $R = R_0$ with velocity given by (2.21) which solves the governing equations once again solves the model equations (2.30) and (2.32); the velocity correction w_1 given in (A 1) is identically zero for this flat solution.

Equation (2.32) coincides with the model studied in Craster & Matar (2006) up to a choice of scalings (and similar to that studied in Kliakhandler *et al.* 2001) with the exception of a sign change in front of $f_2(R;a)$ due to the corresponding sign change in the pressure for the boundary conditions. Craster & Matar (2006) derived their model asymptotically with small Bond number, a derivation which may not be appropriate for all experiments considered here, though these authors comment about the model being possibly valid for Bond numbers higher than those appropriate to their asymptotic assumption (e.g. $Bo = 0.75$). In fact, as we have seen, the same model equation can be derived under different assumptions which are compatible with our experimental regimes. Importantly, all of these models make no assumption about the film being thin relative to the tube or fibre radius. Equation (2.32) fits into a hierarchy of models which will be explored in § 2.4.

It will be shown in the rest of the paper that the first-order model (2.32) captures the most important physical features of the flow and gives good agreement with our experiments. In particular, the stability of steady-state solutions of (2.32) will be analysed in § 4, while the initial-boundary-value problem for this equation will be the focus of our numerical investigations in § 5. It is sometimes more useful to refer to the thickness of the liquid layer $\bar{h} \equiv \bar{a} - \bar{R}$ rather the radius of the air domain $\bar{R}$ as dependent variable; we will display results for the solutions of the long-wave model (2.32) using the variable that best suits the result at hand.

2.3. *Second-order model*

Continuing to the second order allows viscous dispersive effects to be included, and is useful in illustrating how successive iterations of the long-wave model approach the full governing equations in an asymptotic sense. This additional asymptotic step also determines explicitly the lower order $O(\epsilon^2)$ terms neglected in favour of the dominant regularizing term of $O(\epsilon^3)$ from surface tension in (2.19). In this way we can test that, unlike the latter, these additional $O(\epsilon^2)$ terms may not prevent high-curvature regions from developing in sections of the free surface, with the highest-derivative term acting like Korteweg–de Vries (KdV) dispersion (see e.g. Johnson *et al.* 2012 for a mathematical perspective on this point).

At $O(\epsilon^2)$ the equations of motion are

$$p_{2_r} = \frac{1}{r}\partial_r(ru_{1r}) - u_1/r^2 - Re(u_{0t} + u_0u_{0r} + w_0u_{0z}), \tag{2.34}$$

$$\frac{1}{r}\partial_r(rw_{2r}) = -w_{0zz} + p_{1z} + Re(w_{1t} + u_1w_{0r} + u_0w_{1r} + w_0w_{1z} + w_1w_{0z}), \tag{2.35}$$

$$\frac{1}{r}\partial_r(ru_2) + w_{2z} = 0. \tag{2.36}$$

We neglect the inertial effects at this higher-order level. (Even in models where inertial effects are considered to be significant, these second-order terms are often omitted as their effects are not considered critical to the model; see e.g. Ruyer-Quil *et al.* 2008.)

Boundary conditions at the wall $r = a$ are

$$u_2 = w_2 = 0; \tag{2.37}$$

at the interface $r = R(z, t)$ the tangential stress boundary condition is

$$w_{2r} = -u_{0z} + w_{0r}R_z^2 + 2R_z(w_{0z} - u_{0r}). \tag{2.38}$$

The streamwise velocity which solves (2.35), (2.37), and (2.38) is given in the appendix.

The interfacial evolution equation with second-order corrections is

$$R_t = \frac{1}{R}\frac{\partial}{\partial z}\int_R^a (w_0 + \epsilon w_1 + \epsilon^2 w_2) r\mathrm{d}r, \tag{2.39}$$

which can be written (again after neglecting all inertial terms) as

$$R_t = f_1(R; a)R_z + \frac{\epsilon}{R}\left[Sf_2(R; a)(R_z + \epsilon^2R^2R_{zzz}) + \epsilon f_4(R; a)R_z^2 + \epsilon f_5(R; a)R_{zz}\right]_z, \tag{2.40}$$

where f_1 and f_2 are defined in (2.31) and

$$\left.\begin{aligned} f_4(R;a) &= \frac{1}{32R^2}\left[a^6 - 4a^4R^2 + a^2R^4\left(7 - 36\log\frac{R}{a}\right)\right. \\ &\quad \left. + R^6\left(-4 + 40\log\frac{R}{a} - 72\log^2\frac{R}{a}\right)\right], \\ f_5(R;a) &= \frac{1}{32R}\left[-a^6 + a^2R^4\left(9 - 12\log\frac{R}{a}\right)\right. \\ &\quad \left. + R^6\left(-8 + 24\log\frac{R}{a} - 24\log^2\frac{R}{a}\right)\right]. \end{aligned}\right\} \tag{2.41}$$

2.4. *Thin-film limit*

The long-wave model (2.32) has been derived without assuming that the film's thickness is small relative to the tube radius. If the film is taken to be thin, then $\beta = \bar{h}_0/\bar{a} \equiv 1/a \ll 1$ can be taken as a small (film thickness) parameter. This gives $R = a - h = 1/\beta - h$, and (2.32) can be simplified by expanding each of the functions f_i in (2.31) and (2.41)

$$\left.\begin{aligned} f_1 &= -h^2\left(1 - \frac{\beta h}{3}\right) + O(\beta^2), \quad f_2 = -\frac{16\beta h^3}{3}(1+\beta h) + O(\beta^3), \\ f_3 &= -\frac{32h^6}{15\beta} + \frac{268h^7}{63} + O(\beta), \quad f_4 = \frac{7h^3}{3\beta} - \frac{23h^4}{6} + O(\beta), \\ f_5 &= -\frac{h^4}{\beta} + \frac{13h^5}{10} + O(\beta). \end{aligned}\right\} \tag{2.42}$$

If we neglect f_3, f_4, and f_5, we recover

$$(1-\beta h)h_t + \frac{1}{3}\frac{\partial}{\partial z}\left[h^3(1-\beta h)\left(1 + \frac{\epsilon\tilde{S}_F}{a^2(1-\beta h)^2}h_z + \epsilon^3\tilde{S}_F h_{zzz}\right)\right] = 0, \tag{2.43}$$

where $\tilde{S}_F = 16S$. This equation is analogous to the thin-layer fibre-exterior model derived by Roy *et al.* (2002). As these authors pointed out, in the exterior fibre case, this model is still a conservation law for mass. If a very thin film is assumed, i.e. taking the limit $\beta \to 0$, then (2.43) simplifies to the model equation developed by Frenkel (1992),

$$h_t + \frac{1}{3}\frac{\partial}{\partial z}\left[h^3\left(1 + \frac{\epsilon\tilde{S}_F h_z}{a^2} + \epsilon^3\tilde{S}_F h_{zzz}\right)\right] = 0. \tag{2.44}$$

In dimensional form, this equation is

$$\bar{h}_{\bar{t}} + \frac{1}{3\bar{\mu}}\frac{\partial}{\partial\bar{z}}\left[\bar{h}^3\left(\bar{\rho}\bar{g} + \frac{\bar{\gamma}\bar{h}_{\bar{z}}}{\bar{a}^2} + \bar{\gamma}\bar{h}_{\bar{z}\bar{z}\bar{z}}\right)\right] = 0. \tag{2.45}$$

Like the long-wave model, the thin-film model (2.45) has a flat solution, but in contrast to (2.21), $\bar{h} = \bar{h}_0$ does not lead to a velocity profile identical to that of the

governing equations' flat solution (2.6). The thin-film flat velocity profile can be found directly from (2.6) by setting $\bar{r} = \bar{a} - \bar{h}_0 y$ and expanding (2.6) for small β to find

$$\bar{w}_F = \frac{\rho g}{2\mu}(\bar{a} - \bar{r})(2\bar{h}_0 - \bar{a} + \bar{r}). \tag{2.46}$$

There is one subtlety of the thin-film limit worth remarking upon: as $\bar{a} \to \infty$ with fixed $\bar{h}$ in (2.45), the mechanism for instability growth provided by the azimuthal curvature vanishes, in agreement with the case of a flat film. However, note that in the non-dimensional form (2.44) the limit $a \to \infty$ can be achieved both in the previous case and for $\bar{a}$ fixed with $\bar{h} \to 0$. With this latter case, $a \to \infty$ corresponds to an arbitrarily thin film in a cylindrical tube, and the azimuthal curvature remains present as an instability growth mechanism. The thin-film equation (2.44), derived by Frenkel (1992), is also studied by Kerchman & Frenkel (1994) and Kalliadasis & Chang (1994); in the following we will refer to this as the thin-film model or Frenkel model.

Note that (2.44) is a conservation law, but the conserved quantity is now the film thickness h. Thus, the liquid volume or mass is only approximately conserved, as pointed out by Roy *et al.* (2002). It is perhaps unexpected that such a simple approximation of the continuity equation can have surprising consequences. Camassa *et al.* (2012) theoretically and experimentally studied particle trajectories within the film flow for the related problem of core-driven film flow; it was shown there that approximating mass conservation in the thin-film limit artificially alters the steady streamline topology in travelling wave solutions (when viewed in the wave reference frame).

3. Experiments

We designed and conducted a series of experiments to study the gravity-driven film problem. The experimental procedure is described in § 3.1. Experimental data for mean quantities such as film average thickness and fluxes are first examined in § 3.2. Further experimental outcomes on instabilities and their evolution are discussed after the corresponding analytical and numerical model results are introduced in §§ 4 and 5 respectively.

3.1. *Experimental setup and procedures*

Using a Harvard Apparatus Model 975 syringe pump, we provide a constant volume flux of silicone oil into a cylindrical chamber. Once the oil has filled the chamber, it is forced through a radial slit of width 2.5 mm at the top of a pre-wetted 40 cm glass tube. The oil then drains down into the tube, coating the tube axisymmetrically and draining out the bottom of the tube; see figure 2 for a schematic of the set-up.

Tubes of three different inner radii were used for the experiments: 0.5, 0.295, and 0.17 cm. The liquid used was a silicone oil with dynamic viscosity $\mu = 129$ Poise (P) and density $\rho = 0.97$ g cm^{-3} (verified in our lab through an Anton-Paar DMA 4500 densitometer and TA Ares rheometer). The tube radii and liquid viscosity used here are similar to those used in the biologically motivated experiments by Clarke, Jones & Oliver (1970), Kim *et al.* (1986*a*,*b*), and Kim, Iglesias & Sackner (1987). The surface tension of silicone oil with viscosity near $\mu = 129$ P is reported in the literature as $\gamma = 21.5$ dyn cm^{-1}, see e.g. Joseph & Renardy (1993); the Kapitza number of the oil is thus $Ka \approx 3.3 \times 10^{-3}$. The syringe pump was set to a variety of volume flow

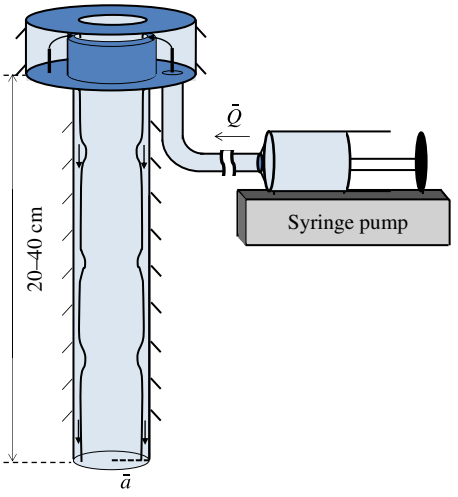

FIGURE 2. (Colour online) Schematic of the experimental test section.

rates for each tube radius. A summary of these experimental parameters is reported in table 1. Note that flow rates for the smallest (0.17 cm) radius tube are significantly lower than those in larger tubes for this value of viscosity, which together with the added difficulty of tracking free-surface features in such small tubes makes for a rather time-consuming and arduous experiment. Accordingly, the data set for this case is smaller than that of the larger radius tubes.

Video images were recorded with a Sony HDR FX1000 video camera. Snapshots of experiments with varying $\bar{Q}$ are shown for $\bar{a} = 0.5$ cm in figure 3. Each experiment was allowed to progress until the film had reached a quasi-steady-state regime, i.e. when the free surface continued to evolve, but on average the evolution did not exhibit any significant changes as more time elapsed. This quasi-steady state was typically achieved within a few minutes. At the end of each experiment, the coated tube was carefully removed from the apparatus and weighed. By comparing the weight of the coated tube with the weight of the same tube when dry, a mean film thickness of the oil was determined. To ensure the robustness of our measured thicknesses, we tested various methods of tube removal and found that all techniques gave weight measurements within 5 % for the same inflow settings and tube radius. Essentially, the high viscosity of the oil ensured minimal drainage during the manipulations needed to determine the tube's weight. The measured average film thicknesses $\bar{h}_0$ corresponding to experimental volume flow rates $\bar{Q}$ are displayed in table 1 for experiments conducted using the 40 cm tubes. Most of the film thicknesses reported are the average of multiple experimental runs. The number of runs conducted for each combination of flow rate and tube radius was dependent on the flow rate for the following reason: for high flow rates, the film exits the tube faster and there is thus a higher degree of uncertainty in the measured thickness due to the weighing procedure described above, while at low flow rates the experiments take longer to conduct but have a lower degree of uncertainty. Thus for thick films and high flow rates, typically three runs were conducted for each combination of flow rate and tube radius, while for thin films and low flow rates, one or two runs were conducted. We also remark that a limited set of experiments, not reported in this table, was also carried out with a longer 1 m tube of radius $\bar{a} = 0.5$ cm to further test the evolution

0.5 cm		$\bar{a}$: 0.295 cm		$\bar{a}$: 0.17 cm	
$\bar{Q}$ (cm^3 s^{-1})	$\bar{h}_0$ (cm)	$\bar{Q}$ (cm^3 s^{-1})	$\bar{h}_0$ (cm)	$\bar{Q}$ (cm^3 s^{-1})	$\bar{h}_0$ (cm)
8.9×10^{-3}	0.117	8.6×10^{-4}	0.066		
1.2×10^{-2}	0.131	1.2×10^{-3}	0.071		
1.7×10^{-2}	0.149	1.6×10^{-3}	0.081		
2.6×10^{-2}	0.170	2.3×10^{-3}	0.092	2.2×10^{-4}	0.048
3.4×10^{-2}	0.194	3.3×10^{-3}	0.108	3.1×10^{-4}	0.051
4.8×10^{-2}	0.223	4.6×10^{-3}	0.120	4.3×10^{-4}	0.055
6.7×10^{-2}	0.256	6.3×10^{-3}	0.131	5.9×10^{-4}	0.066
9.4×10^{-2}	0.295	8.9×10^{-3}	0.152	8.6×10^{-4}	0.073
1.3×10^{-1}	0.331	1.2×10^{-2}	0.189	1.2×10^{-3}	0.092
1.8×10^{-1}	0.398	1.7×10^{-2}	0.249	1.6×10^{-3}	0.123
1.81×10^{-1}	0.500	2.19×10^{-2}	0.295	2.42×10^{-3}	0.170

TABLE 1. Experimental volume flow rate $\bar{Q}$ and measured average film thickness $\bar{h}_0$ for each experiment with the 40 cm tube having the given inner radius. For reference, the last row reports the theoretical flux values corresponding to Poiseuille gravity-driven full-pipe flow, $\bar{h}_{0_P} = \bar{a}$ (or $\bar{R}_0 = 0$), and $\bar{Q}_P = \pi\rho g\bar{a}^4/8\mu$.

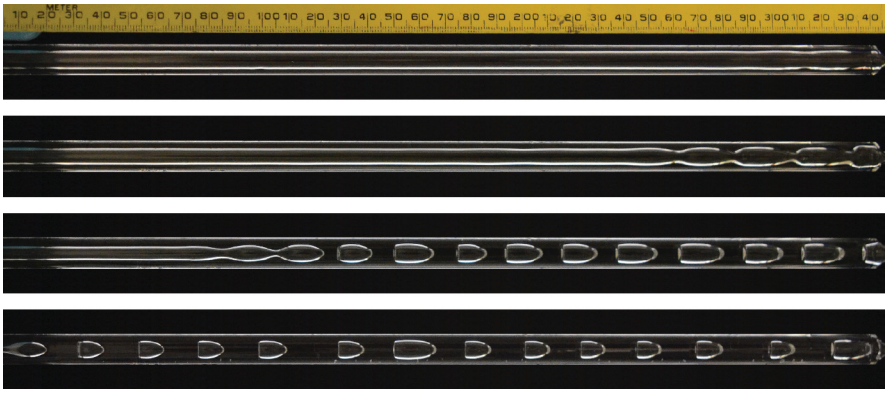

FIGURE 3. (Colour online) Snapshots of four experiments with $\mu = 129$ P and $\bar{a} = 0.5$ cm. (*a*) $\bar{Q} = 4.8 \times 10^{-2}$ cm^3 s^{-1}, (*b*) $\bar{Q} = 6.7 \times 10^{-2}$ cm^3 s^{-1}, (*c*) $\bar{Q} = 9.4 \times 10^{-2}$ cm^3 s^{-1}, and (*d*) $\bar{Q} = 1.3 \times 10^{-1}$ cm^3 s^{-1}. (This montage of tube snapshots is rotated by 90° with respect to the actual experiment, so that acceleration due to gravity g acts from left to right.)

of convective instability. For this longer tube, a high-precision Harvard Apparatus Ph.D. Ultra Hpsi syringe pump was used to improve the resolution of volume fluxes around the appropriate parametric region of interest discussed in § 5.

3.2. *Experimental results and volume averages*

The liquid flux generated by the flat exact solution (2.6) for each film thickness is given by

$$\bar{Q} \equiv 2\pi \int_{\bar{R}_0}^{\bar{a}} \bar{w}(\bar{r})\, \bar{r}\, \mathrm{d}\bar{r} = \frac{\pi\rho g}{8\mu}\left(\bar{a}^4 - 4\bar{a}^2\bar{R}_0^2 + 3\bar{R}_0^4 - 4\bar{R}_0^4 \log\frac{\bar{R}_0}{\bar{a}}\right). \tag{3.1}$$

Thus, for a given flux $\bar{Q}$, this expression can be inverted to yield an exact solution, $\bar{R} = \bar{R}_0(\bar{Q})$, of the Navier–Stokes equations when the interface of the falling annular liquid film in the vertical tube remains flat. Note that the velocity $\bar{w}$ of the exact solution (2.6) for a flat interface is also the leading-order velocity for the long-wave model, and hence this flat solution $\bar{R}_0(\bar{Q})$ coincides with an exact flat-interface solution of the long-wave model, so that equation (3.1) is also the leading-order flux for the long-wave model.

For thin films $1 - \bar{R}_0/\bar{a} \ll 1$ (or $\bar{h}_0/\bar{a} \ll 1$), a Taylor expansion shows that the flux can be approximated by

$$\bar{Q}_F = \frac{2\pi\rho g\bar{a}}{3\mu}(\bar{a} - \bar{R}_0)^3. \tag{3.2}$$

This expression for the thin-film flux $\bar{Q}_F$ also follows directly from

$$\bar{Q}_F = 2\pi\bar{a}\int_{\bar{R}_0}^{\bar{a}} \bar{w}_F(\bar{r})\,\mathrm{d}\bar{r}, \tag{3.3}$$

with $\bar{w}_F$ given in (2.46).

Note that in the limit $\bar{R}_0 \to 0$ (or $\bar{h}_0 \to \bar{a}$), the theoretical expression for flow rate in Poiseuille pipe flow under gravity is recovered from (3.1), i.e.

$$\bar{Q}_P \equiv \lim_{\bar{R}_0 \to 0} \bar{Q} = \frac{\pi\rho g\bar{a}^4}{8\mu}, \tag{3.4}$$

which establishes the maximum flux sustainable by the pure hydrostatic pressure jump due to the liquid's weight in the tube. Higher flux rates after the tube is entirely filled from the inlet downward would require an additional pressure source above the inlet, or a depression at the outlet.

Figure 4 groups the flux-thickness pairs found in the experiments compared with those given by (3.1) and (3.2); both theoretical predictions are displayed for $0 \leqslant \bar{Q} \leqslant \bar{Q}_P$. For both thin films and moderately thick films the match between experiments and (3.1) is rather accurate, while agreement between experiments and (3.2) is generally found only for thin films; this is not surprising since in our experiments the film mean thicknesses were not overly small and thus should lie outside of the asymptotic assumptions for (3.2). The lack of precise agreement between (3.1) and experiments for thick films is expected in light of the snapshots in figure 3: thick films in the experiment form liquid bridges or plugs and thus are dynamically far from the flat-interface exact solution. Note that while increasing film thickness always corresponds to increasing volume flux, both the experiments and exact solution exhibit an inflection point; on the exact solution curve, this inflection point occurs at $\bar{h}_0 \approx 0.614\bar{a}$, a condition readily found from (3.1). This is due to the cylindrical geometry of the tube: for thick films, an incremental increase in film thickness adds less fluid than the same increase for a thin film. No such inflection point exists in (3.2).

Similar comparisons can be made between experiments, long-wave model (2.32), and thin-film model (2.44). In the models, mass (long-wave models), or film thickness (thin-film model), is prescribed by the initial condition, and the volume flux is allowed to vary freely as the solution evolves in time. In the experiments, the opposite is true: volume flux is prescribed and the mean thickness settles to some value in the quasi-steady-state regime. Hence, the volume flux associated with each film thickness

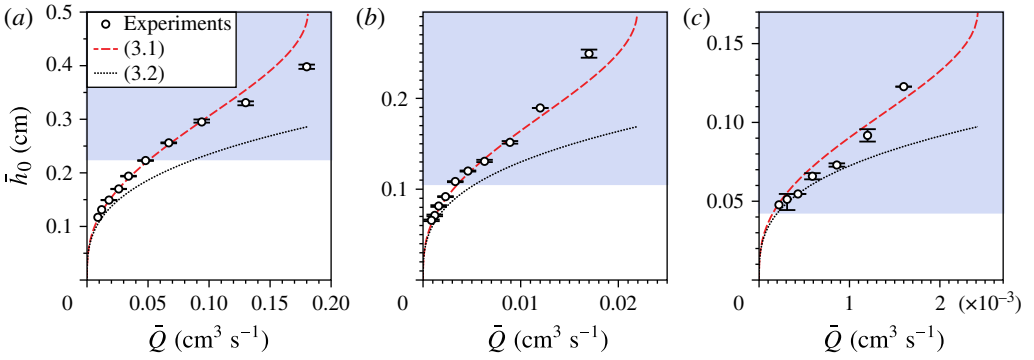

FIGURE 4. (Colour online) Comparison of volume flux and mean film thickness for $\mu = 129$ P and (*a*) $\bar{a} = 0.5$ cm, (*b*) $\bar{a} = 0.295$ cm, and (*c*) $\bar{a} = 0.17$ cm. Bars indicate the range of measured thicknesses recorded over multiple runs for each experiment. For the two thinnest films in (*a*) and the thinnest film in (*c*), only one run was conducted. Theoretical predictions (3.1) (dashed line) and (3.2) (dotted line) are also shown. Shaded regions correspond to thick films for which numerical solutions to the long-wave model do not settle into a quasi-steady state.

in the long-wave model has to be determined *a posteriori* by allowing the solution to evolve until the spatially averaged volume flux has settled to some constant value. For relatively thin films, quasi-steady regimes are quickly reached and the interfacial disturbances maintain a small amplitude throughout the evolution, thus indicating that the total volume flux can be well-approximated by the leading-order flux in the small long-wave parameter ϵ. Hence, the corresponding flux values are observed to be very close to those of the exact (flat) solution of both long-wave model and the parent Navier–Stokes equations (2.6) and (3.1), and the corresponding $\bar{h}_0$ versus $\bar{Q}$ curves in the non-shaded regions in figure 4 are indistinguishable from the exact flat solution (and hence are not reported in this figure).

We remark that predictions from our models only hold for parameter values such that the numerical solutions reach a quasi-steady regime, whereby time evolution is no longer transient. Those thicknesses for which solutions to the long-wave model did not reach such a regime are indicated by the shaded regions in figure 4. This point will be discussed further in § 5, where we will see that lack of a quasi-steady regime for the long-wave model past a certain film thickness can be correlated to plug formation. It is also interesting to note that the flat solution (3.1) continues to predict fairly accurate film thicknesses for given fluxes long past the onset of plug-formation regimes. This could be viewed as a manifestation of the robustness of the mass conservation law versus the local dynamics of the free surface. Such robustness is also reflected in the long-wave model's overall good agreement with experiments, for as long as the model is viable (which corresponds to absence of plugs in the experiment). This marks a contrasting difference with respect to the non-mass-conserving thin-film model.

4. Linear stability analysis

Flat-film solutions, common to both parent equations and their asymptotic models, can be expected to be unstable to perturbations, and depending on the set-up their linear regime growth can be broadly classified as temporal or spatial instability. We examine both these cases next.

4.1. *Temporal stability analysis*

The starting point for linear stability analysis is common to all the models considered so far (i.e. thin-film (2.44), first- (2.32) and second- (2.40) order long-wave models) and relies on the assumption of the flat-interface solution being slightly perturbed by a superposition of Fourier modes

$$R = (a-1) + A\exp[\mathrm{i}(kz-\omega t)], \tag{4.1}$$

where $A \ll a-1$ is the amplitude of the disturbance. For temporal stability, we assume that this amplitude is assigned initially as a function of the real wavenumber k. For (4.1) to be a solution, the frequency ω is assigned by (a branch of) the dispersion relation, or $\omega = W(k)$. Then $\mathrm{Re}[W]/k$ is the phase speed of the perturbation, and $\mathrm{Im}[W]$ is its growth or decay rate. Substituting (4.1) into (2.44), (2.32) and (2.40) and neglecting higher-order terms in A gives the dispersion relation for each of the models

$$\omega_F = k + \mathrm{i}\epsilon S_F\left(\frac{k^2}{a^2} - \epsilon^2 k^4\right), \tag{4.2}$$

$$\begin{aligned}\omega_1 = {} & \frac{1}{2}\left(a^2 - (a-1)^2 - 2(a-1)^2\log\frac{a}{a-1}\right)k + \mathrm{i}\epsilon S(a-1)^3 \\ & \times\left[\left(\frac{a}{a-1}\right)^4 - 4\left(\frac{a}{a-1}\right)^2 + 3 + 4\log\frac{a}{a-1}\right]\left[\frac{k^2}{(a-1)^2} - \epsilon^2 k^4\right],\end{aligned} \tag{4.3}$$

$$\begin{aligned}\omega_2 = {} & \frac{1}{2}\left(a^2 - (a-1)^2 - 2(a-1)^2\log\frac{a}{a-1}\right)k \\ & + \frac{\epsilon^2}{32(a-1)}\left[-a^6 + a^2(a-1)^4\left(9 - 12\log\frac{a-1}{a}\right)\right. \\ & \left. + (a-1)^6\left(-8 + 24\log\frac{a-1}{a} - 24\log^2\frac{a-1}{a}\right)\right]k^3 + \mathrm{i}\epsilon S(a-1)^3 \\ & \times\left[\left(\frac{a}{a-1}\right)^4 - 4\left(\frac{a}{a-1}\right)^2 + 3 + 4\log\frac{a}{a-1}\right]\left[\frac{k^2}{(a-1)^2} - \epsilon^2 k^4\right],\end{aligned} \tag{4.4}$$

respectively for thin-film, first- and second-order long-wave models (and $S_F \equiv \tilde{S}_F/3$). Note that (4.2) and (4.3) are similar to that of the Kuramoto–Sivashinsky (KS) equation in their polynomial dependence on k, while (4.4) is similar to that of the Korteweg–de Vries/Kuramoto–Sivashinsky (KdV–KS) equation as studied by e.g. Johnson *et al.* (2012). Also note that the wavenumber of the instability which undergoes maximum growth in the thin-film model is $k_m = 1/(\epsilon a\sqrt{2})$, while in the long-wave models this wavenumber is $k_m = 1/\epsilon(a-1)\sqrt{2}$. Thus, for the thin-film model the wavelength of maximum growth rate is determined by the tube radius, whereas in both long-wave models the average radius of the free surface plays the determining role. (We note that in Craster & Matar 2006 the model by Frenkel 1992 was rescaled in the axial direction by a/R. While this is asymptotically equivalent to the original aspect ratio for large a and results in significant improvement in the agreement between long-wave and thin-film models in this limit, we choose here to use the thin-film scaling as originally introduced by Frenkel 1992.)

For viscous-dominated flows the governing equations of motion reduce to the well-known Stokes approximation. A linear stability analysis can be carried out in closed

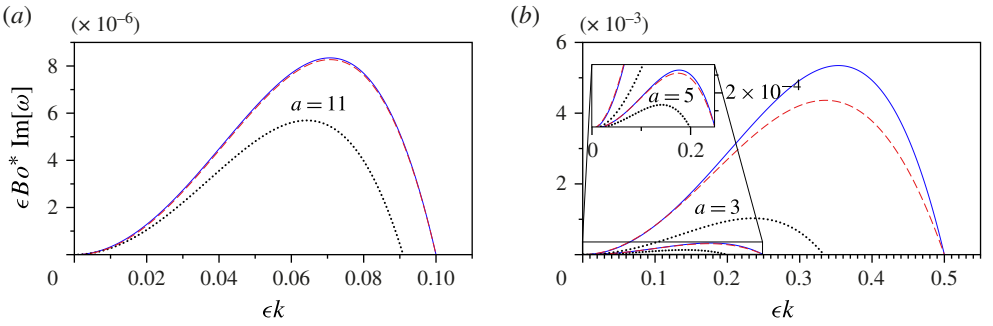

FIGURE 5. (Colour online) The growth rates predicted by linear analysis of the long-wave models (solid lines), the thin-film model (dotted lines), and the Stokes equations (dashed lines) are shown for (*a*) $a = 11$ and (*b*) $a = 5$ and $a = 3$.

form for the flat free-surface solutions of this system, and it is largely independent of whether the interior or the exterior case is considered. Rather than repeating the analysis here, we simply recall that the dispersion relation for the Stokes system can be expressed in terms of Bessel functions, and refer to Goren (1962) and Craster & Matar (2006) for details in the analogous exterior case. Figure 5 shows the growth rates (4.2)–(4.4) and the growth rate of the full Stokes equations. In figure 5(*a*) the growth rates are shown for $a = 11$ corresponding to a relatively thin film; in figure 5(*b*) the growth rates are shown for $a = 5$ and $a = 3$ corresponding to thicker films which lie outside the regime where the asymptotic assumptions made in deriving the thin-film model hold. As expected, the growth rates of the long-wave and thin-film models approach the Stokes equations asymptotically for small k. The maximum growth rate for each model is

$$\mathrm{Im}[\omega_F] = \frac{S_F}{4\epsilon a^4}, \tag{4.5}$$

$$\mathrm{Im}[\omega_1] = \frac{S}{4\epsilon(a-1)}\left[\left(\frac{a}{a-1}\right)^4 - 4\left(\frac{a}{a-1}\right)^2 + 3 + 4\log\left(\frac{a}{a-1}\right)\right], \tag{4.6}$$

where $\mathrm{Im}[\omega_1]$ is the maximum growth rate for both long-wave models. Note that the maximum growth rate of the thin-film model is significantly less than that of both the long-wave model and Stokes equations even for thin films (large a).

Figure 6 shows the wavelength of maximum growth rate. The thin-film model selects a wavelength based on tube radius rather than mean film thickness, while the wavelength decreases with film thickness in the long-wave model and Stokes equations. Experimental results are also shown for those experiments in which instability growth was consistently visible in the linear regime. Wavelengths were measured from the first visible wave crest to the next crest occurring down the tube; the video recording of the experiment was then advanced until this wavelength had progressed down the tube and another wavelength had become visible. This process was repeated, and the average of all such wavelengths for one realization of the experiment is shown with error bars depicting one standard deviation. The small number of data points shown reflects the fact that for high values of volume flux instabilities grow outside the linear regime almost immediately upon entering the tube, while low values of volume flux produce instabilities of very small amplitude and are thus difficult to identify.

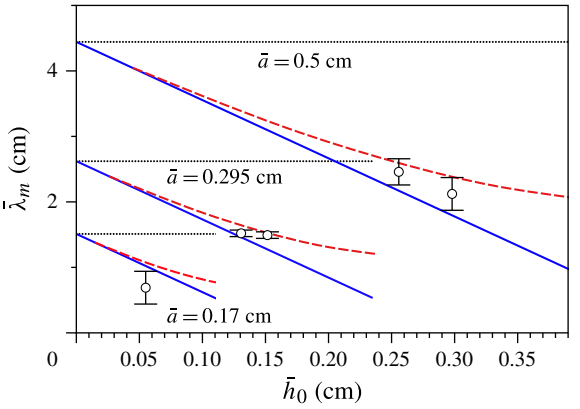

FIGURE 6. (Colour online) The wavelength $\bar{\lambda}_m$ of maximum growth rate predicted by linear analysis of the long-wave models (solid lines), the thin-film model (dotted lines), the Stokes equations (dashed lines), and experiments (circles) are shown. Error bars indicate the standard deviation. Data are only shown for those experiments in which instabilities were consistently visible in the linear regime.

The data shown for $\bar{a} = 0.17$ cm should be viewed with these difficulties in mind, as instabilities progressed quickly in space from the linear to nonlinear regime making it difficult to consistently determine a wavelength without a substantial improvement of optical resolution; we leave further studies in such small geometries for the future.

Figure 7 compares the linear disturbance speed of all three models and the Stokes equations. In figure 7(*a*) disturbance speeds are shown for $a = 5$ and $a = 3$ while in figure 7(*b*) speeds are shown for $a = 2$ and $a = 1.5$; these values of a correspond to relatively thick films for which the thin-film asymptotic assumptions do not hold. The first-order long-wave model has no dispersion, and the speed of a linear disturbance of any wavelength is exactly the speed of the Stokes equations in the limit $k \to 0$, as expected. The second-order long-wave model includes viscous dispersive effects, and this correction gives speed predictions very close to the full Stokes equations for a larger band of small wavenumbers k. Note that the speed of a linear disturbance in the thin-film model is always higher than its counterparts in the long-wave models and in the Stokes equations.

4.2. *Absolute and convective instabilities*

The experiments performed here can be categorized by the location in the tube where instability growth can be visually detected. For thin films, instability growth is first visible far away from the inlet as in figure 3(*a–c*), and the exact spatial location of where instabilities are first visible varies significantly as the experiment progresses. For thicker films, instabilities are consistently visible very close to the inlet, as in figure 3(*d*). Films which only exhibit visible instability growth far away from the inlet are said to be convectively unstable, while those which exhibit growth very near to the inlet are classified as absolutely unstable (see Duprat *et al.* 2007 for a discussion of this classification in the case of an exterior coating).

This instability classification is borrowed from the literature concerning jets and has been well studied. Films which coat the exterior of a fibre have been shown to be absolutely unstable if the fibre has small enough radius and the film thickness

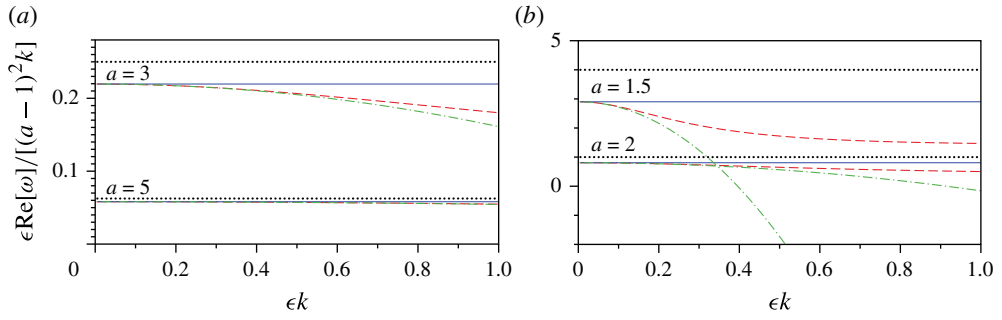

FIGURE 7. (Colour online) The speed of an infinitesimal disturbance predicted by linear analysis of the first-order long-wave model (solid lines), the second-order long-wave model (dot-dashed lines), the thin-film model (dotted lines), and the Stokes equations (dashed lines) for (*a*) $a = 5$ and $a = 3$ and (*b*) $a = 2$ and $a = 1.5$.

lies in some intermediate range (which is determined by the fibre radius and liquid properties); for fibres of large enough radius the exterior coating is always convectively unstable, regardless of the film thickness (Duprat *et al.* 2007). We now explore the same question for films coating the interior of a tube.

The appropriate tools for this study are centred around the asymptotic analysis of Fourier-type integrals (see e.g. Erdelyi 1956 and Whitham 1974), and have been developed by e.g. Briggs (1964) and Bers (1983), and further reviewed by Huerre & Monkewitz (1990). A thorough exposition of these tools would transcend the purpose of our study, and we only mention here the essential elements for completeness, referring the reader to the cited literature for a full discussion. In this approach to asymptotic stability, the normal-mode analysis conducted in § 4.1 is extended by considering complex wavenumbers. The space–time asymptotic behaviour of a perturbation obtained by Fourier superposition of modes (4.1) is determined by the complex solutions $k = \kappa(m)$ ('saddle points') of the equation $\partial_k W = m \equiv x/t$ along a given ray $m = \text{const.}$ for a branch of the dispersion relation $\omega = W(k)$. In a Fourier integral solution with respect to wavenumber k, the asymptotics is then obtained by deforming the original integration for real k to a path in the complex k-plane following steepest descent curves through saddle points $\kappa(m)$ with commensurate, growth or decay, exponential behaviour along a given ray. Accordingly, at a fixed location x, the long-time behaviour is determined by the study along the ray $m = 0$ of the saddle point $\kappa(0) \equiv \kappa_a$ defined by $\partial_k W|_{k=\kappa_a} = 0$. The most amplified mode among all acceptable κ_a values then governs the long-time behaviour; if $\mathrm{Im}[W(\kappa_a)] > 0$ the instabilities are said to be absolute since the envelope of the Fourier superposition would then be stationary in space and exponentially growing in amplitude as time progresses. Acceptable saddle points κ_a are determined by a selection criterion, which corresponds to requiring that the original Fourier integration on the real k-axis can be smoothly deformed to a 'steepest descent' path $\mathrm{Im}[W(k)] = \mathrm{Im}[W(\kappa_a)]$ threading through each saddle point κ_a. This selection criterion can in turn be interpreted in terms of different forms of coalescence of branches of the dispersion relation, see e.g. Huerre & Monkewitz (1990) for further discussion.

For our experimental set-up, perturbations can be assumed to originate at the inlet slit and be continuously fed through the liquid lines. Mathematically, this corresponds to a time-dependent perturbation applied as boundary forcing at the inlet location of the tube. When this perturbing time-dependent forcing is viewed as a superposition

of Fourier oscillatory modes $\exp(\mathrm{i}\Omega t)$, the response of the fluid system may be decomposed into a combination of transient time-dependent behaviour, corresponding to the temporal stability analysis above, and spatially evolving solutions tuned to the real forcing frequency Ω. Convective instability gives rise to a transient time evolution that eventually dies out at every fixed spatial location along the tube, as the unstable growing envelope moves away (and out of the tube) with non-zero group velocity. Thus, if only convective instability is present, only spatially growing (unstable) modes tuned to the forcing frequency of the form $\exp[\mathrm{i}(K(\Omega)z - \Omega t)]$ are left to be observed in the tube after sufficiently long times. Here the complex values $k = K(\Omega)$ are given by the branches of the inverse of the dispersion relation such that $\mathrm{Im}[K(\Omega)] < 0$, which implies spatial growth and propagation down the tube ($z > 0$) when the phase speed $\Omega/\mathrm{Re}[K(\Omega)] > 0$ is positive. Conversely, when absolute instability is present, these spatially growing modes play a secondary role as they are eventually swamped by the time-dependent growth at any fixed spatial location along the tube, and in particular at the inlet location $z = 0$.

Duprat *et al.* (2007) found that for the exterior problem and the thin-film model (2.44) there is a critical value S_{F_c} such that for $S_F > S_{F_c}$ the film is absolutely unstable, and for $S_F < S_{F_c}$ the film is convectively unstable. Adjusting for the choice of scalings used here, the critical value is in our case

$$S_{F_c} = \frac{a^3}{2}(-17 + 7\sqrt{7})^{1/2} \approx 0.617a^3. \tag{4.7}$$

Expressed in terms of the experimental parameters, the condition $S_F > S_{F_c}$, required for the film to be absolutely unstable according to the thin-film model, is

$$\bar{R}_0 < \bar{a} - \frac{3(-17 + 7\sqrt{7})^{1/2}\rho g \bar{a}^3}{2\gamma}. \tag{4.8}$$

As noted in Duprat *et al.* (2007), the thin-film dispersion relation (4.2) can be transformed into the first-order long-wave dispersion relation (4.3) by the transformation

$$\omega = -\frac{a-1}{f_1(a-1;a)a}\omega', \quad k = \frac{a-1}{a}k', \quad S_F = \frac{a^3 f_2(a-1;a)}{(a-1)^2 f_1(a-1;a)}S'. \tag{4.9}$$

Therefore, applying (4.9) to the condition $S_F > S_{F_c}$ yields the following implicit condition for absolute instability in the long-wave model:

$$\frac{1}{\bar{R}_0^2}\frac{f_2\left(\dfrac{\bar{R}_0}{\bar{a}-\bar{R}_0};\dfrac{\bar{a}}{\bar{a}-\bar{R}_0}\right)}{f_1\left(\dfrac{\bar{R}_0}{\bar{a}-\bar{R}_0};\dfrac{\bar{a}}{\bar{a}-\bar{R}_0}\right)} > \frac{8\rho g(-17+7\sqrt{7})^{1/2}}{\gamma}. \tag{4.10}$$

Figure 8 shows the regions of absolute versus convective instability for interior coatings as predicted by (4.8) and (4.10), for the thin-film and long-wave models respectively, compared with experimental results. The long-wave model shows good agreement with our experiments. Note that the thin-film model predicts that for tubes with radius greater than $\bar{a} \approx 0.11$ cm all films are convectively unstable. (This property of the thin-film model to predict convective instabilities in a larger region of parameter

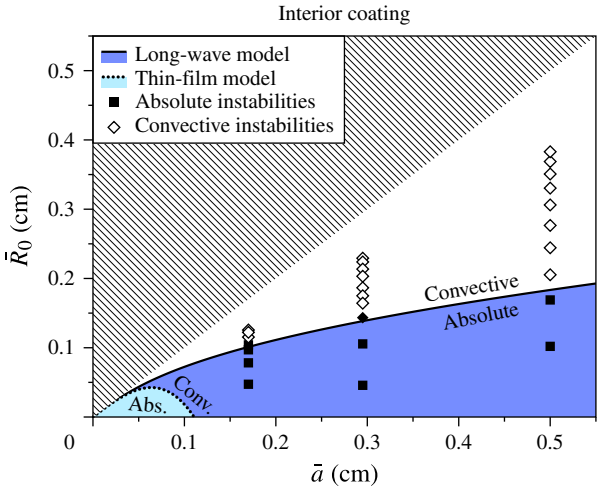

FIGURE 8. (Colour online) Regions of absolute and convective instability for the long-wave model (solid lines) and the thin-film model (dotted lines). Shaded regions (blue online) correspond to regions of absolute instability for the corresponding model. Liquid properties are $\gamma = 21.5$ dyn cm^{-1} and $\rho = 0.97$ g cm^{-3} corresponding to experiments in § 3. (The closed diamond indicates a film thickness where the flow exhibited both absolute and convective instability at some point during the experiment.)

space is consistent with the overestimate of the linear wave speed and underestimate of the maximum growth rate when compared to the long-wave models and Stokes equations.)

Before proceeding to nonlinear results for the tube case, we note that for the exterior case Duprat *et al.* (2007) show that the thin-film model (2.44) predicts that absolute instabilities are present independently of the size of the fibre, provided the film thickness is large enough. On the other hand, the long-wave model in Craster & Matar (2006) predicts a critical fibre radius (as a function of liquid properties) beyond which instabilities can only be convective. This is the opposite of the situation for interior coatings, as just discussed, though in both cases the long-wave model accurately captures the stability of the film. For comparison with the interior case, we show in figure 9 the counterpart of our results for the fibre coating case, after a rescaling of the results in figure 4 in Duprat *et al.* (2007) to match the choice of scalings used in our work.

5. Nonlinear results

Having analytically explored the linear stability of small-amplitude perturbations, we now study the nonlinear saturation of instabilities numerically. This allows us to follow the evolution from a perturbed flat initial state to regimes where quasi-steady wavetrains emerge, or, conversely, where there is no evidence that these long-time quasi-steady regimes seem to take hold. We remark that the one-to-one relation between flux and interface (3.1) is modified by the evolution of the instabilities, so that the flux Q becomes a function of time t and spatial location z along the tube. Hence, the flux spatial average

$$\langle Q \rangle \equiv \frac{2\pi}{L} \int_0^L \int_{R(z,t)}^a \big(w_0(r,t) + \epsilon w_1(r,t)\big)\, r\, \mathrm{d}r\, \mathrm{d}z, \tag{5.1}$$

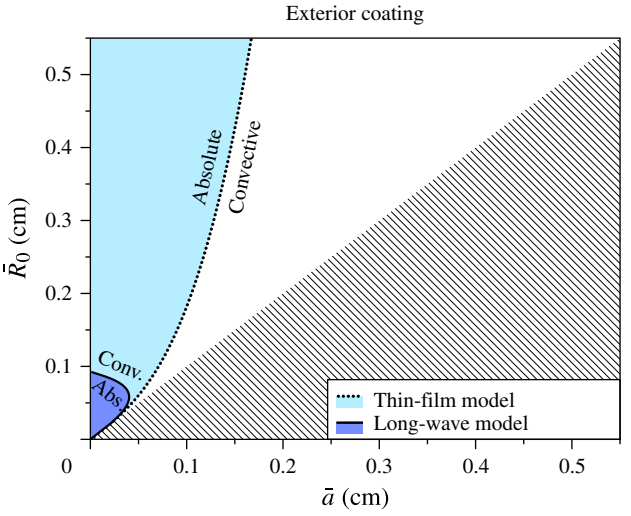

FIGURE 9. (Colour online) Same as figure 8 but for a film coating the exterior of the fibre (i.e. $\bar{R}_0 > \bar{a}$), as shown in Duprat *et al.* (2007).

is in general a time-dependent function. Even under the periodic boundary conditions (used in our simulations), which make the spatial mean of $(R(z, t))^2$ a constant of time due to (2.15), the explicit expression for w_1 (see the appendix, (A 1)) and the long-wave model (2.33) show that $\langle Q \rangle$ is time dependent, in general. Nonetheless, numerical solutions reveal that whenever a quasi-steady regime is reached, the spatial average of flux $\langle Q \rangle$ and mean thickness $\langle R^2 \rangle$ track curves which are virtually indistinguishable from their flat-solution counterparts shown in figure 4.

5.1. *Transient solutions*

The long-wave model (2.32) is solved using the method of lines with a pseudospectral algorithm (whereby spatial derivatives are calculated in Fourier space and the nonlinear terms are computed in physical space). Time integration uses a simple second-order predictor–corrector scheme. Throughout the simulations, the Fourier modes of the derivatives and nonlinear terms were carefully monitored to ensure conservation of volume. For initial conditions, we perturb the interface with multiple small-amplitude modes (see Camassa *et al.* 2012 for more details of the numerical procedure on a related problem).

The numerical solutions fall into one of two categories. For films with mean thickness smaller than some critical value depending on $\bar{a}$, i.e. $\bar{h}_0 < \bar{h}_c(\bar{a})$, the interface evolves into a series of small-amplitude waves. Figure 10(*a*) shows an example of such a free-surface evolution by plotting a sequence of snapshots of the free-surface profile $\bar{h}(\bar{z}, \bar{t})$ at fixed time increments. Successive snapshots of the interface are shown; the perturbed interface sees instability growth which saturates into small-amplitude waves. These waves undergo some limited nonlinear interaction before settling into a series of stable travelling waves. This behaviour is reminiscent of similar equations studied more extensively in the literature. For example, the dispersion relation for the long-wave model was seen to be of Kuramoto–Sivashinsky (KS) type in § 4, and solutions to the KS equation are well-known to exhibit

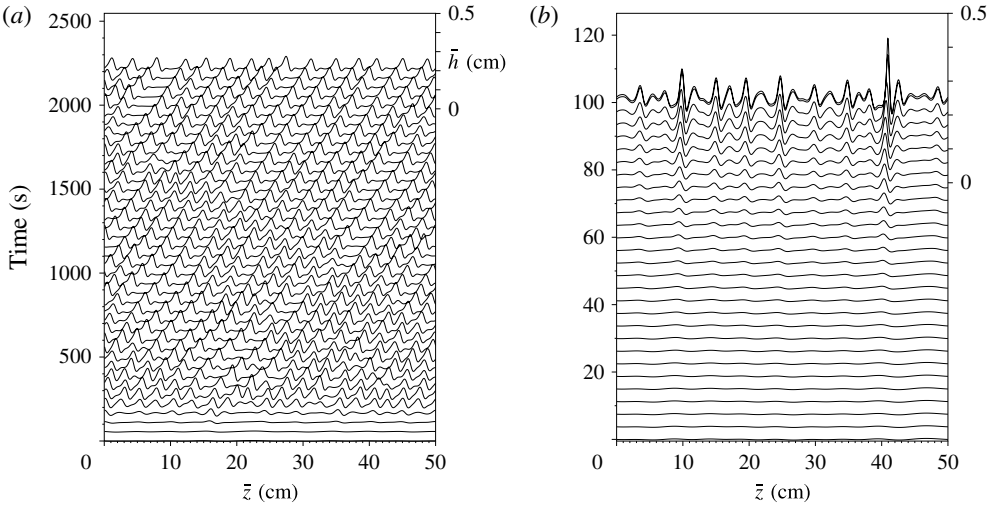

FIGURE 10. Time snapshots showing the evolution of solutions to (2.32) in a periodic domain for $\bar{a} = 0.5$ cm. Interfacial profiles $\bar{h}(\bar{z}, \bar{t})$ are shown successively shifted at time intervals $\Delta\bar{t}$. Profiles are shown in the frame of reference moving with an undisturbed interface. The scale for $\bar{h}$ is given on the right-hand axis for the final profile shown. Acceleration due to gravity acts from left to right. (*a*) $\bar{R}_0 = 0.2766$ cm, $\Delta\bar{t} \approx 55$ s, (*b*) $\bar{R}_0 = 0.2443$ cm, $\Delta\bar{t} \approx 3.75$ s. (For the final profile in (*b*), $\Delta\bar{t} \approx 0.56$ s.)

spatio-temporal chaos. It has also been shown that adding dispersive terms to the KS equation can regularize the evolution (see e.g Johnson *et al.* 2012 for a study of the KdV–KS equation). Likewise, the fully nonlinear model studied here contains dispersive terms which become significant as instabilities grow beyond the linear regime, and which appear to regularize the free-surface evolution allowing coherent wave structures to form.

For thicker films with $\bar{h}_0 > \bar{h}_c(\bar{a})$, there is numerical evidence that the model can break down with some form of finite-time blow-up. In figure 10(*b*), a perturbed interface once again experiences instability. This time, however, the instability with largest amplitude undergoes rapid growth to the point of becoming comparable to the tube's radius, or $\bar{R}(\bar{z}, \bar{t}) = 0$ at some time $\bar{t}$ and location $\bar{z}$ in the periodic domain, indicating a tendency for the liquid to 'choke' the tube and form a liquid plug. When this approach to $\bar{R} = 0$ occurs, some of the coefficients of the long-wave model (2.32) become large, leading to a very stiff problem which requires smaller and smaller time-steps. We do not attempt here to provide a full mathematical characterization of this blow-up trend, leaving it to future work. Of course, the model ceases to be valid as extra physical phenomena not modelled by our long wave-asymptotics would come into play as the air domain pinches off, and diametrically opposite locations along the interface come into contact. Nonetheless, it is natural to take the tendency for the interface location $\bar{h}$ to limit to $\bar{a}$, and equivalently $\bar{R} \to 0$, as an indication of the formation of a liquid plug.

Next, we test this 'choke' criterion for plug formation based on the numerical integration of model (2.32) against the experimental observation. Just as with the model solutions, experimental films with mean thickness smaller than some critical value do not exhibit plug formation, while thicker films do. A comparison between model prediction and experimental evidence is summarized in figure 11, where both

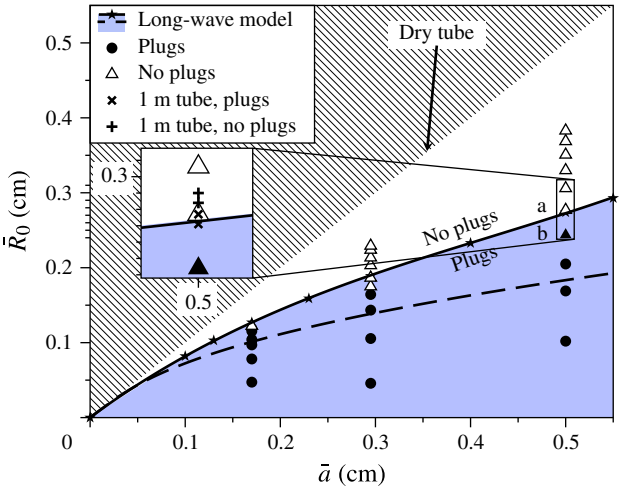

FIGURE 11. (Colour online) Shaded region (blue online) shows parametric space for mean interfacial thickness $\bar{R}_0$ and tube radius $\bar{a}$ (40 cm long) resulting in plug formation, as numerically determined by the blow-up criterion at points $(\bar{a}, \bar{R}_0)$ marked by '$\star$' (boundary curve is least-square fit on cubic polynomial). Experimental results are shown with circles (plugs form) and triangles (no plugs). Points 'a' and 'b' correspond to the values used in figures 10(*a* and 10*b*) respectively, as well as the experimental snapshots seen in figures 3(*a* and 3*b*) respectively. (The closed triangle marking point 'b' indicates that some, but not all, instabilities formed plugs before exiting the tube.) Inset shows data from the 1 m long tube experiment, by zooming in on the transition region between plug and no plug formation. Dash curve marks the separation between absolute and convective instability depicted in figure 8 and determined by relation (4.8).

the experimental data and model solutions are classified according to the existence of plug formation. The numerical data are interpolated with a least-square fit on a cubic polynomial, giving rise to the empirical curve $\bar{R}_0 = \mathcal{R}(\bar{a})$ depicted by the solid line in figure 11, which we take as the model prediction for the boundary between plug and no-plug regimes.

A remarkably good agreement can be seen between the long-wave model predictions and experimental observations reported in figure 11, where the plug regime is indicated by the shaded area (blue online) below curve $\mathcal{R}(\bar{a})$ in the parametric plane $(\bar{a}, \bar{R}_0)$. The boundary between convective and absolute instability, analytically determined by (4.8), is also depicted in this figure by a dashed curve, showing how absolute instability may be a sufficient but not necessary criterion for plug formation. It is interesting to note that the sectorial region between these two curves corresponds to where the model predicts that liquid plugs (i.e. bridges in the two-dimensional image projection) will form, but only after the instabilities have traversed a considerable distance (from the feeding chamber in the experimental case).

In the bulk of our experiments, we are limited to observing plug or bridge formation in the first 40 cm of distance travelled; it is quite possible that instabilities would eventually form in the experimental regimes corresponding to this parameter range, if the tube were long enough to allow for the growth and interaction of the unstable modes. To check on this, we have performed a limited set of experiments around the critical regime for a 1 m long tube with 0.5 cm radius, which are about the maximal dimensions that our current experimental set-up can handle. The additional data points

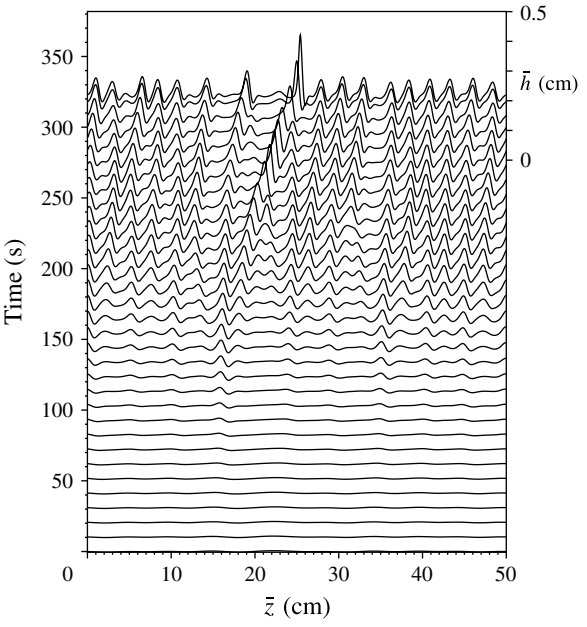

FIGURE 12. Same as figure 10 but with $\bar{R}_0 = 0.27$ cm and $\Delta\bar{t} \approx 10.3$ s. (For the final profile, $\Delta\bar{t} \approx 4.9$ s.)

thus gathered are explicitly marked in the inset of figure 11, and further narrow the experimental transition region between plug/no-plug regimes for this largest diameter tube. (Because of the length, the average film thickness for this 1 m tube is computed through interpolation by using the data and curve(s) reported in figure 4(*a*) rather than by weight.) We remark that in the transition region the model solutions show that bridge formation occurs as the result of nonlinear interactions between waves, as opposed to the growth of a single wave crest, which appears to be a different amplitude-increase mechanism than that exhibited in figure 10; this is exemplified by figure 12 by matching fluid parameters and mean thickness intermediate between those chosen for figures 10(*a*) and 10(*b*). It is also interesting to note the similarity between curves separating different regions of the $(\bar{a}, \bar{R}_0)$-plane in figures 8 and 11, again stressing the existence of the narrow region of parameter space where instabilities are convective and do form plugs. While it would be difficult to explore experimentally, this region of convective and plug-forming instability may persist in the limit of small radii, though not visible in the scales of figure 11. An example of this combination of flow attributes in an experimental result can be seen in figure 3(*c*).

A few remarks are in order concerning the numerical computations. The model equation is solved using periodic boundary conditions, clearly not corresponding to the experiment set-up. Hence, in order to emulate more closely the spatial growth of the instabilities observed in the experiments, we tested the model again with periodic boundary conditions, but this time using an extended domain (dimensionally corresponding to 150 cm), which makes the computation more expensive. The initial conditions of the previous section, i.e. a flat interface perturbed by small-amplitude disturbances of many modes, were modified in the following way. First, the flat interface was perturbed by the wavenumber $\bar{k}_m$ mode with highest growth rate that satisfies the periodic boundary conditions as determined from the linear stability

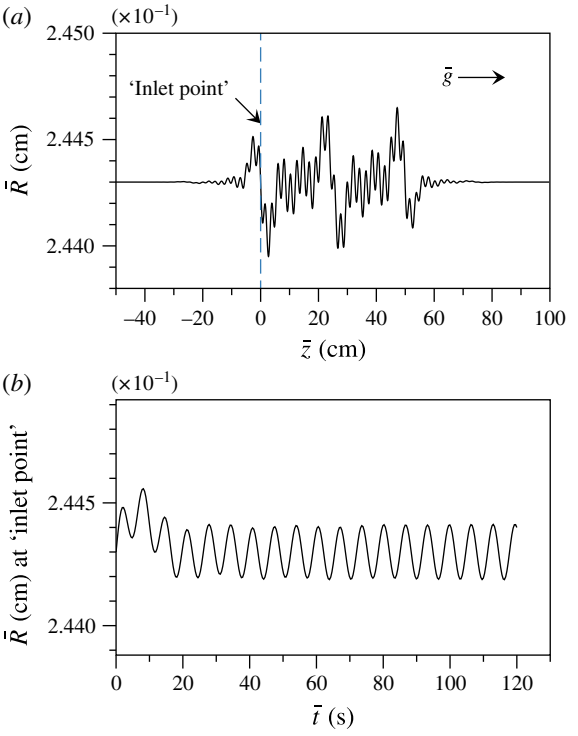

FIGURE 13. (*a*) Initial condition (5.2) with $N = 3$, for model solutions shown in figure 14(*b*). (*b*) The location of the free surface at the 'inlet point' shown in (*a*) as a function of time.

analysis in § 4.1; some additional modes with smaller wavenumber were also added to the perturbed interface. Second, upstream from an arbitrarily chosen 'inlet point' this perturbed interface was damped exponentially by a factor corresponding to this maximum growth rate $\mathrm{Im}[\bar{W}(\bar{k}_m)]$ which we analytically determined as described in § 4.1. For example, figure 13(*a*) shows one such initial condition given by

$$\bar{R} = \bar{R}_0 - \bar{A} f(\bar{z}) \sin(\bar{k}_m \bar{z}) - \bar{A} f(\bar{z}) \sum_{n=1}^{N} \sin\left(\frac{12\pi n \bar{z}}{\bar{L}}\right), \tag{5.2}$$

where $\bar{L} = 150$ cm is the computational domain length, $\bar{R}_0 = 0.2443$ cm, $\bar{A} = 10^{-4}$ cm, $\bar{k}_m \approx 2.89$, $N = 3$, and the envelope function f is

$$f(\bar{z}) = \begin{cases} \exp[\bar{\alpha}\,\bar{z}], & \bar{z} \leqslant 0 \\ 1, & 0 < \bar{z} < 2\bar{z}_0 \\ \exp[-\bar{\alpha}(\bar{z} - 2\bar{z}_0)], & \bar{z} \geqslant 2\bar{z}_0. \end{cases} \tag{5.3}$$

Here the scale factor $\bar{\alpha} > 0$ is the spatial rate of growth for propagating disturbances (cf. § 4.2), the envelope is centred at $\bar{z}_0 = 25$ cm, $\bar{\alpha} \equiv -\bar{k}_m\, \mathrm{Im}[\bar{W}(\bar{k}_m)]/\mathrm{Re}[\bar{W}(\bar{k}_m)]$ and the origin of the vertical coordinate is chosen so that $\bar{z} = 0$ corresponds to the inlet point.

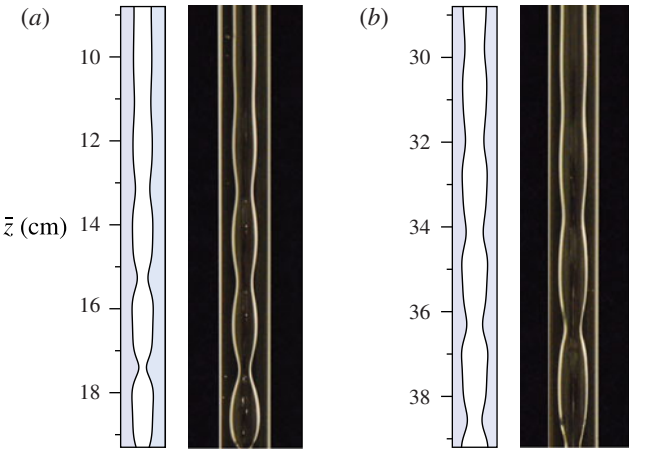

FIGURE 14. (Colour online) Model solutions (left) and experiments (right) for $\bar{a} = 0.5$ cm and for (*a*) $\bar{Q} = 9.4 \times 10^{-2}$ cm^3 s^{-1} and (*b*) $\bar{Q} = 6.7 \times 10^{-2}$ cm^3 s^{-1}. The initial condition for the model solution in (*b*) is shown in figure 13(*a*).

The evolution of these initial conditions proceeds along the lines discussed in § 4.2: an initial time transient occurs where the wavelength of maximum growth rate is selected by the model and begins to dominate the free surface, followed by a later time evolution where the instabilities reaching the 'inlet point' have nearly constant amplitude and frequency $\bar{\Omega} = \mathrm{Re}[\bar{W}(\bar{k}_m)]$. In this way the numerical inlet point $\bar{z} = 0$ serves as an approximation to the actual inlet feeding location in our experiments, for as long as the wrap around of wavetrains due to the finite periodic domain does not affect the solution near $\bar{z} = 0$. Figure 13(*b*) shows the thickness of the film at the inlet point as time elapses using the initial condition shown in figure 13(*a*).

Figure 14 compares solutions for two different thicknesses (for different volume fluxes) with corresponding experiments, showing a reasonable qualitative match. Note that in the experimental snapshots the bright line should be interpreted as only an approximate indication of the location of the free surface. Optical distortions from the combination of curved interfaces of liquid and tube wall, due to the differences in the refraction index, would have to be compensated for a precise evaluation of distances. (Also note that these difficulties in determining the exact location of the free surface do not arise in the case of exterior flows.) Thus, here we simply take the bright curves in the experimental frames to be approximately representative of the deformation of the free surface, and leave further quantitative comparisons to future work.

5.2. *Travelling waves*

Some solutions to (2.32) show the existence of stable, coherent wave structures propagating down the tube as in figure 10(*a*). To explore their behaviour further we now turn to a numerical study of travelling wave solutions of the evolution equation (2.32).

Switching to a frame of reference that travels with the wave, we let

$$Z = z - ct. \tag{5.4}$$

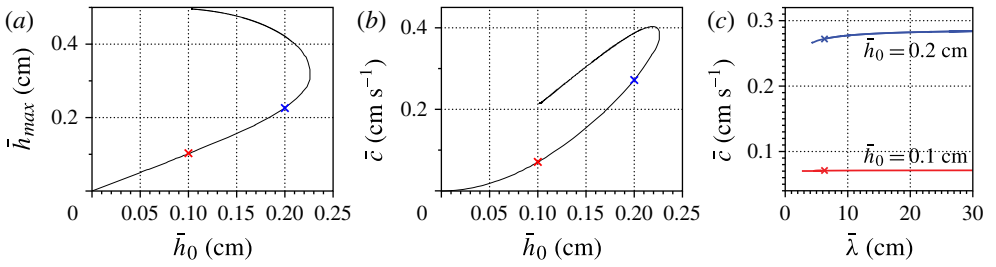

FIGURE 15. (Colour online) Travelling wave solution branches (fluid parameters matching those in the experiments). (*a*) Maximum thickness as a function of mean thickness. (*b*) Speed as a function of mean thickness. (*c*) Speed as a function of domain length, using parameters corresponding to those in the solutions marked by an 'x' in (*a*) and (*b*).

Substituting (5.4) into (2.32) yields a fourth-order ordinary differential equation

$$-cR' = f_1(R;a)R' + \frac{\epsilon S}{R}\frac{\mathrm{d}}{\mathrm{d}Z}\left[f_2(R;a)(R' + \epsilon^2 R^2 R''')\right]; \tag{5.5}$$

for reference we also include the dimensional form of (5.5)

$$-\mu\bar{c}\bar{R}' = \rho g f_1(\bar{R};\bar{a})\bar{R}' + \frac{\gamma}{16\bar{R}}\frac{\mathrm{d}}{\mathrm{d}\bar{Z}}\left[f_2(\bar{R};\bar{a})(\bar{R}' + \bar{R}^2\bar{R}''')\right]. \tag{5.6}$$

As (5.5) is not directly solvable, we seek solutions numerically in the following way. By first solving the evolution equation (2.32) and letting the solution settle to a steady series of travelling waves, we obtain a train of nearly identical pulses. We then use one pulse of the evolution solution with an appropriate domain length as the seed in an iterative scheme based on a collocation-method two-point boundary-value problem solver. Throughout the iterative steps, we continue to enforce conservation of volume; see Camassa *et al.* (2012) for details of this method. To explore how the properties of these solutions change as we adjust parameter values, the continuation software AUTO07 was used to trace out solution branches (Doedel *et al.* 2008).

Curves of amplitude and speed as functions of the mean film thickness $\bar{h}_0$ for travelling wave solutions thus determined are shown in figure 15, with $\mu =$ 129 P and $\bar{a} = 0.5$ cm. As seen in figure 15(*a*,*b*), for very thin films the peak wave amplitude increases in an almost linear fashion while the speed increases approximately quadratically. As the thickness of the film increases, amplitude and speed increase until the film approaches a critical thickness, $\bar{h}_c \approx 0.227$ cm. Past this (bifurcation) point, the solution curves double back giving rise to a second branch of travelling wave solutions. For decreasing film thickness, the upper portion of these curves corresponds to solutions whose amplitude continues to increase while the corresponding speed decreases except for a small neighbourhood of the bifurcation point. Note that this value of $\bar{h}_c$ corresponds almost exactly to the value $\bar{h}_0 = \bar{a} - \bar{R}_0$, for the case $\bar{a} = 0.5$ cm, which distinguishes plug formation from wavy interface as seen in figure 11. It is interesting to conjecture that the lack of a travelling-wave solution branch for values of mean thickness $\bar{h}_0$ larger than the critical value $\bar{h}_c$ could signal plug formation in the actual experiment, but more work needs to be done for an in-depth verification of this. Also left to further investigation is the issue of stability of solutions along the upper and lower portions of the solution curve,

corresponding, as figure 15(*a*,*b*) shows, to multiple wave forms for the same set of experimental parameters and mean film thickness. As a preliminary test on the stability of these solutions, we used them as initial conditions in the evolution model (2.32). In each case the wave retained its shape as it propagated through several domain lengths. However, while the lower branch of the solution curve seems to act as a sort of attractor in time-dependent simulations starting from slightly perturbed flat-interface initial conditions, the high-amplitude solutions do not seem to ever be attained in any of the simulations we performed for the same class of initial data. Furthermore, it remains to be seen just how sensitive these higher-amplitude solutions are to perturbations other than those generated by numerical error.

We remark that for decreasing mean film thicknesses, solutions corresponding to the upper branch in figure 15(*a*) have peak amplitudes that increase to plug-formation levels, or $\bar{h}_{max} \to \bar{a}^-$. This could be viewed as a sort of time-independent route to bridge or plug formation supported by the model. However, this is not likely to be of physical relevance as this class of travelling waves, unlike its lower-amplitude counterpart, does not seem to play a role in any of the evolutions out of generic initial conditions that we simulated numerically.

It is also interesting to study properties of solutions along branches as parameters other than mean thickness are varied. For instance, for fixed experimental parameter values and fixed $\bar{h}_0$, it can be seen that wave speed is largely insensitive to the size of the periodic domain $\bar{\lambda}$. In fact, as this increases, the wave speed seems to approach a constant, c_∞ say, as in figure 15(*c*). However, while all solutions shown in figure 15(*c*) contain a single wave crest within a period, it is unclear whether in the limit $\bar{\lambda} \to \infty$ this can be maintained, that is, whether true solitary wave solutions exist for the model.

Finally, in order to better understand how the fluid mass is flowing in each of the two forms of solution for given mean thickness $\bar{h}_0$, we reconstruct the stream function from the velocity field,

$$u = -\partial_z \Psi, \quad w - c = \frac{1}{r}\partial_r(r\Psi), \tag{5.7}$$

where in the first-order model, $w = w_0 + \epsilon w_1$, $u = u_0 + \epsilon u_1$. Integrating (5.7) gives

$$\begin{aligned}\Psi \;=\; & \left[-\frac{1}{4} + \frac{4\epsilon S}{R^2}(R_z + \epsilon^2 R^2 R_{zzz})\right]\left[\frac{1}{4r}(a^2 - r^2)^2\right] \\ & + \left[\frac{R^2}{2} - 8\epsilon S(R_z + \epsilon^2 R^2 R_{zzz})\right]\left[\frac{1}{4r}\{a^2 - r^2 + 2r^2\log(r/a)\}\right].\end{aligned} \tag{5.8}$$

We then plot isolines of the stream function Ψ. Figure 16 shows streamlines for two of these solutions which have identical mean thickness. Note that in figure 16(*b*) a small region of closed streamlines near the wave crest exists, indicating the presence of a recirculation zone, or trapped core of fluid which rolls over the rest of the substrate layer; solutions which lie on the dashed line (blue online) in figure 16(*a*) all exhibit this property. In figure 16(*c*) no such trapped core exists; all solutions which lie on the solid line (red online) in figure 16(*a*) exhibit this property. This has consequences on the type of transport that tracers in the fluid would experience, as illustrated by Camassa *et al.* (2012).

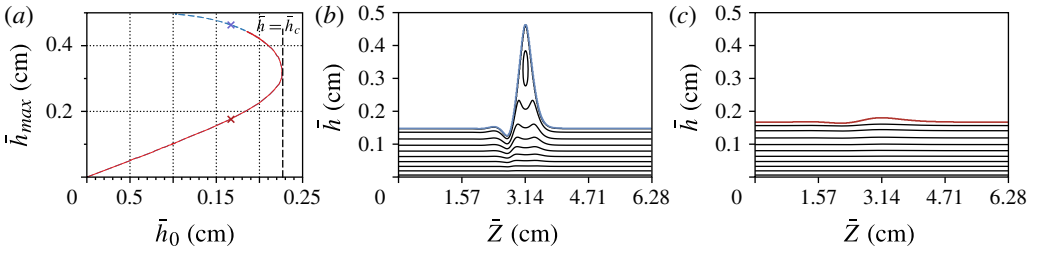

FIGURE 16. (Colour online) Travelling wave solutions (fluid parameters matching those in the experiments) shown in the periodic box (0, 6.28 cm). (*a*) Same as 15(*a*); each 'x' corresponds to solutions with identical mean thickness. Solutions lying along the dashed line (blue online) contain a trapped core of fluid when viewed in the travelling reference frame; solutions lying along the solid line (red online) do not. (*b*,*c*) Streamlines plotted in a frame of reference moving with the wave. In (*b*), the closed streamlines indicate the presence of a trapped core; (*c*) contains only open streamlines.

6. Discussion

We have carried out an experimental and modelling investigation of gravity-driven flows of viscous films coating the inner wall of a vertical tube. We have developed and analysed a series of models based on long-wave asymptotics, and tested their predictions against the experimental data we have collected. For the range of parameters we have explored in our experiments, we have found that a first-order model which neglects the fluid's inertia adequately captures most of the key dynamics, in both linear (small free-surface deformation) and nonlinear (large deformations close to clogging) regimes. We have carried out a linear stability analysis of our model and compared the results for both existing models and Stokes equations for viscous-dominated flows. In particular, we have found that both the model and experiments indicate that for any tube size there exists a film thickness large enough to become absolutely unstable. This is in contrast with the exterior coating problem which has received most of the attention in the literature. Our model predicts this critical film thickness with reasonable accuracy. The numerical simulations of the model further illustrate how the (many) nonlinear terms of the model govern the saturation of instabilities. Further, these simulations estimate thicknesses which lead to the formation of plugs in the tube. We have also numerically determined branches of travelling wave solutions and followed their bifurcations. These are found to provide an organizing principle behind the plug formation in the tube, as these branches exhibit critical points at thicknesses corresponding to values for which both numerical solutions and experiments show evidence of liquid plugs.

It was demonstrated by Smolka *et al.* (2008) that the model derived by Craster & Matar (2006) accurately describes the flow of an exterior coating in the linear regime. Our study shows that the interior counterpart (2.32) of a similar first-order long-wave model derived for interior coating performs just as well in the presence of an arguably richer set of dynamical outcomes. Thus, the model offers reliable predictions for the additional physical phenomena for the interior case, and can therefore be used as an effective tool for predicting the motion of interior liquid coating in the corresponding asymptotic parametric range.

Our study establishes the building block for related problems, such as the case of the air occupying the core region of the tube being no longer stationary but forced to flow by an imposed pressure gradient. In the upcoming Part 2 of the current work, the

effects of turbulent air flow on the free surface of a highly viscous film coating the interior of a tube will be considered. The model developed in Camassa & Lee (2006) and Camassa *et al.* (2012) will be updated to include additional corrective terms to improve the accuracy in modelling the free-surface evolution.

Acknowledgements

This project derives from the Virtual Lung Project at UNC. We thank Greg Forest for many illuminating discussions, Michael Jenkinson for his earlier contributions to the modelling and experimental effort, and Girard Iervolino, Chris Joy, Jeeho Kim, and Leandra Vicci for their contributions with the experiments throughout this study. This research was supported by NSF DMS-0509423, DMS-0908423, DMS-1009750, RTG DMS-0943851, CMG ARC-1025523 and NIEHS 534197-3411.

Appendix. Long-wave asymptotics details

The solution to (2.24)–(2.28) is

$$\left.\begin{aligned} u_1(r,z,t) &= \frac{1}{16Bo\,R^3 r}\left[2(a^2-r^2)^2R_z^2+4\left(a^2-r^2+2r^2\log\frac{r}{a}\right)R^4R_zR_{zzz}\right.\\ &\quad -R\left((a^2-r^2)^2-2\left(a^2-r^2+2r^2\log\frac{r}{a}\right)R^2\right)(R_{zz}+R^2R_{zzzz})\Big]\\ &\quad +g_{11}(r,R;a)R_z^2+g_{12}(r,R;a)R_{zz},\\ w_1(r,z,t) &= \frac{1}{4\,Bo}\left(r^2-a^2-2R^2\log\left(\frac{r}{a}\right)\right)\left(\frac{R_z}{R^2}+R_{zzz}\right)+g_{21}(r,R;a)R_z,\\ p_1(r,z,t) &= \frac{1}{2R}\left(a^2-R^2-2R^2\log\frac{r}{a}\right)R_z, \end{aligned}\right\} \tag{A 1}$$

where each function $g_{ij}(r,z,t)$ is

$$\begin{aligned} g_{11}(r,z,t) &= Re\frac{1}{768r}\left[-13a^6+33a^4r^2-21a^2r^4+r^6+12a^2r^4\log\frac{r}{a}\right.\\ &\quad +6R^2\left(-17a^4+48a^2r^2-31r^4+12a^2r^2\log\frac{r}{a}+32r^4\log\frac{r}{a}-12r^4\right.\\ &\quad \times\left(\log\frac{r}{a}\right)^2+\log R\left(-6a^4+6a^2r^2-12a^2r^2\log\frac{r}{a}\right)-36a^4\log\frac{R}{a}\\ &\quad +60a^2r^2\log\frac{R}{a}-30r^4\log\frac{R}{a}-24a^2r^2\log\frac{r}{a}\log\frac{R}{a}+24r^4\log\frac{r}{a}\\ &\quad \times\log\frac{R}{a}+2a^2\log a\left(3a^2+2r^2+6r^2\log\frac{R}{a}\right)+6a^2r^2\log\frac{R}{r}-2a^2r^2\\ &\quad \times\log r\left(5+6\log\frac{R}{r}\right)\Big)-6R^4\left(a^2-r^2+2r^2\log\frac{r}{a}\right)\\ &\quad \times\left.\left.\left(-19-4\log\frac{R}{a}+40\left(\log\frac{R}{a}\right)^2\right)\right], \end{aligned} \tag{A 2}$$

$$
\begin{aligned}
g_{12}(r,z,t) \;=\; & Re\frac{R}{768r}\Bigg[-13a^6+33a^4r^2-21a^2r^4+r^6+12a^2r^4\log\frac{r}{a}\\
& -6R^2\Bigg(a^4-8a^2r^2+31r^4-8a^2r^2\log\frac{r}{a}-8r^4\log\frac{r}{a}+4r^4\left(\log\frac{r}{a}\right)^2\\
& +\log R\left(2a^4-2a^2r^2+4a^2r^2\log\frac{r}{a}\right)+12a^4\log\frac{R}{a}-20a^2r^2\log\frac{R}{a}\\
& +10r^4\log\frac{R}{a}+8a^2r^2\log\frac{r}{a}\log\frac{R}{a}-8r^4\log\frac{r}{a}\log\frac{R}{a}-2a^2\\
& \times\log a\left(a^2+2r^2\log\frac{R}{a}\right)-2a^2r^2\log\frac{R}{r}+2a^2r^2\log r\left(1+2\log\frac{R}{r}\right)\Bigg)\\
& -6R^4\left(a^2-r^2+2r^2\log\frac{r}{a}\right)\left(-3-4\log\frac{R}{a}+8\left(\log\frac{R}{a}\right)^2\right)\Bigg], \qquad \text{(A 3)}
\end{aligned}
$$

$$
\begin{aligned}
g_{21}(r,z,t) \;=\; & Re\frac{1}{128}\Bigg[R\left(-11a^4+12a^2r^2-r^4-8a^2r^2\log\frac{r}{a}\right)\\
& +R^3\left(-20(a^2-r^2)-24r^2\log\frac{r}{a}+16r^2\left(\log\frac{r}{a}\right)^2\right)\\
& +a^2R^3\left(-16\log\frac{r}{a}-8\log a\log\frac{R}{a}+8\log r\log\frac{R}{r}+8\log R\log\frac{r}{a}\right)\\
& +R^3\log\frac{R}{a}\left(32(r^2-a^2)+16a^2\log\frac{r}{a}-32r^2\log\frac{r}{a}\right)\\
& -12R^5\log\frac{r}{a}-16R^5\log\frac{r}{a}\log\frac{R}{a}+32R^5\log\frac{r}{a}\left(\log\frac{R}{a}\right)^2\Bigg]. \qquad \text{(A 4)}
\end{aligned}
$$

The second-order axial velocity which solves (2.35), (2.37), and (2.38) is

$$
\begin{aligned}
w_2(r,z,t) \;=\; & \frac{1}{8R^2}\left(a^4-a^2r^2+3R^2(r^2-a^2)+4r^2R^2\log\frac{a}{r}+36R^4\log\frac{a}{r}\log\frac{a}{R}\right)R_z^2\\
& +\frac{1}{8R}\Bigg(-a^4+a^2r^2+3R^2(r^2-a^2)+4(r^2+R^2)R^2\log\frac{a}{r}\\
& +12R^4\log\frac{a}{r}\log\frac{a}{R}\Bigg)R_{zz}. \qquad \text{(A 5)}
\end{aligned}
$$

REFERENCES

BERS, A. 1983 Space–time evolution of plasma instabilities-absolute and convective. In *Handbook of Plasma Physics* (ed. M. N. Rosenbluth & R. Z. Sagdeev), vol. I, pp. 451–517. North-Holland.

BRIGGS, R. J. 1964 *Electron-Stream Interaction With Plasmas*. MIT Press.

CAMASSA, R., FOREST, M. G., LEE, L., OGROSKY, H. R. & OLANDER, J. 2012 Ring waves as a mass transport mechanism in air-driven core-annular flows. *Phys. Rev.* E **86**, 066305.

CAMASSA, R. & LEE, L. 2006 In *Advances in Engineering Mechanics – Reflections and Outlooks* (ed. A. Chwang, M. Teng & D. Valentine), pp. 222–238. World Scientific.

CAMPANA, D. M., UBAL, S., GIAVEDONI, M. & SAITA, F. 2007 Stability of the steady motion of a liquid plug in a capillary tube. *Ind. Engng Chem. Res.* **46**, 1803–1809.

CLARKE, S. W., JONES, J. G. & OLIVER, D. R. 1970 Resistance to two-phase gas-liquid flow in airways. *J. Appl. Physiol.* **29**, 464–471.

CRASTER, R. V. & MATAR, O. K. 2006 On viscous beads flowing down a vertical fibre. *J. Fluid Mech.* **553**, 85–105.

CRASTER, R. V. & MATAR, O. K. 2009 Dynamics and stability of thin liquid films. *Rev. Mod. Phys.* **81**, 1131–1198.

DOEDEL, E. J., CHAMPNEYS, A. R., DERCOLE, F., FAIRGRIEVE, T., KUZNETSOV, Y., OLDEMAN, B., PAFFENROTH, R., SANDSTEDE, B. J., WANG, X. & ZHANG, C. 2008 *AUT0-07P: Continuation and Bifurcation Software for Ordinary Differential Equations*. Montreal Concordia University.

DUPRAT, C., RUYER-QUIL, C., KALLIADASIS, S. & GIORGIUTTI-DAUPHINE, F. 2007 Absolute and convective instabilities of a viscous film flowing down a vertical fiber. *Phys. Rev. Lett.* **98**, 244502.

ERDELYI, A. 1956 *Asymptotic Expansions*. Dover.

FRENKEL, A. L. 1992 Nonlinear theory of strongly undulating thin films flowing down vertical cylinders. *Europhys. Lett.* **18**, 583–588.

GOREN, S. L. 1962 The instability of an annular thread of fluid. *J. Fluid Mech.* **27**, 309–319.

HALPERN, D. & GROTBERG, J. B. 1992 Fluid-elastic instabilities of liquid-lined flexible tubes. *J. Fluid Mech.* **244**, 615–632.

HAMMOND, P. S. 1983 Nonlinear adjustment of a thin annular film of viscous fluid surrounding a thread of another within a circular cylindrical pipe. *J. Fluid Mech.* **137**, 363–384.

HICKOX, C. 1971 Instability due to viscosity and density stratification in axisymmetric pipe flow. *Phys. Fluids* **14**, 251–262.

HUERRE, P. & MONKEWITZ, P. A. 1990 Local and global instabilities in spatially developing flows. *Annu. Rev. Fluid Mech.* **22**, 473–537.

JENSEN, O. E. 2000 Draining collars and lenses in liquid-lined vertical tubes. *J. Colloid Interface Sci.* **221**, 38–49.

JOHNSON, M. A., NOBLE, P., RODRIGUES, L. M. & ZUMBRUN, K. 2012 Spectral stability of periodic wave trains of the Korteweg–de Vries/Kuramoto–Sivashinsky equation in the Korteweg–de Vries limit. arXiv:1202.6402v1.

JOSEPH, D. D. & RENARDY, Y. 1993 *Fundamentals of Two-Fluid Dynamics, Part 2: Lubricated Transport, Drops, and Miscible Liquids*. Springer.

KALLIADASIS, S. & CHANG, H.-C. 1994 Drop formation during coating of vertical fibres. *J. Fluid Mech.* **261**, 135–168.

KERCHMAN, V. I. & FRENKEL, A. L. 1994 Interactions of coherent structures in a film flow: simulations of a highly nonlinear evolution equation. *Theor. Comput. Fluid Dyn.* **6**, 235–254.

KIM, C. S., RODRIGUEZ, C. R., ELDRIDGE, M. A. & SACKNER, M. A. 1986*a* Criteria for mucus transport in the airways by two-phase gas-liquid flow mechanism. *J. Appl. Physiol.* **60**, 901–907.

KIM, C. S., GREENE, M. A., SANKARAN, S. & SACKNER, M. A. 1986*b* Mucus transport in the airways by two-phase gas-liquid flow mechanism: continuous flow model. *J. Appl. Physiol.* **60**, 908–917.

KIM, C. S., IGLESIAS, A. J. & SACKNER, M. A. 1987 Mucus clearance by two-phase gas-liquid flow mechanism: asymmetric periodic flow model. *J. Appl. Physiol.* **62**, 959–971.

KLIAKHANDLER, I. L., DAVIS, S. H. & BANKOFF, S. G. 2001 Viscous beads on vertical fibre. *J. Fluid Mech.* **429**, 381–390.

LIN, S. P. & LIU, W. C. 1975 Instability of film coating of wires and tubes. *AIChE J.* **24**, 775–782.

LISTER, J. R., RALLISON, J. M., KING, A. A., CUMMINGS, L. J. & JENSEN, O. E. 2006 Capillary drainage of an annular film: the dynamics of collars and lobes. *J. Fluid Mech.* **552**, 311–343.

ORON, A., DAVIS, S. H. & BANKOFF, S. G. 1997 Long-scale evolution of thin liquid films. *Rev. Mod. Phys.* **69**, 932–980.

ROY, R. V., ROBERTS, A. J. & SIMPSON, M. E. 2002 A lubrication model of coating flows over a curved substrate in space. *J. Fluid Mech.* **454**, 235–261.

RUYER-QUIL, C., TREVELEYAN, P., GIORGIUTTI-DAUPHINE, F., DUPRAT, C. & KALLIADASIS, S. 2008 Modelling film flows down a fibre. *J. Fluid Mech.* **603**, 431–462.

SMOLKA, L., NORTH, J. & GUERRA, B. 2008 Dynamics of free surface perturbations along an annular viscous film. *Phys. Rev.* E **77**, 036301.

SURESH, V. & GROTBERG, J. B. 2005 The effect of gravity on liquid plug propagation in a two-dimensional channel. *Phys. Fluids* **17**, 031507.

UBAL, S., CAMPANA, D. M., GIAVEDONI, M. D. & SALTA, F. A. 2008 Stability of the steady-state displacement of a liquid plug driven by a constant pressure difference along a prewetted capillary tube. *Ind. Engng Chem. Res.* **47**, 6307–6315.

WHITHAM, G. B. 1974 *Linear and Nonlinear Waves*. Wiley.

YIH, C.-S. 1967 Instability due to viscosity stratification. *J. Fluid Mech.* **27**, 337–352.